Interface Engineering and Defect Tolerance in $RbSnBr_3$ Perovskite Solar Cells: A Numerical Analysis of HTL Impact

Abdul Mateen Arshad[1], A. Ali[*1], Mohsin M. Tarar[2], Mohsin Ali[1], SU Rahman[3]
[1]Department of Physics, University of Chakwal
[2]Department of Electronics Engineering, University of Chakwal
[3]Department of Mathematics, University of Chakwal
*Correspondence: azmat.chakwal@gmail.com

Citation | Arshad. A. M, Ali. A, Tarar. M. M, Ali. M, Rahman. S. U, "Interface Engineering and Defect Tolerance in $RbSnBr_3$ Perovskite Solar Cells: A Numerical Analysis of HTL Impact", IJIST, Vol. 8 Issue. 7 pp 3050-3083, September 2026
DOI:
Received | Sep 06, 2026 **Revised |** Sep 22, 2026 **Accepted |** Sep 25, 2026 **Published |** Sep 28, 2026.

This work presents a systematic SCAPS-1D investigation of the influence of five hole transport layers (HTLs), namely CuSCN, Cu_2O, P3HT, PTAA, and PEDOT:PSS, on the interface energetics, charge transport, defect tolerance, and photovoltaic performance of lead-free $RbSnBr_3$ perovskite solar cells employing the FTO/SnS_2/ $RbSnBr_3$/ HTL/ Au device architecture. To isolate the intrinsic influence of HTL properties, all device parameters, interfaces, and operating conditions were kept identical except for the HTL material. Unlike conventional HTL-screening studies that primarily compare photovoltaic performance, the present work integrates analyses of energy-band alignment, current–voltage (J–V), quantum efficiency (QE), capacitance–voltage (C–V), conductance–voltage (G–V), density of states, carrier mobility, contact engineering, bulk and interface defects, and temperature-dependent characteristics to establish the physical relationship between HTL properties and device operation. PEDOT: PSS and P3HT exhibited comparable simulated photovoltaic performances, achieving power conversion efficiencies (PCEs) of 22.87% and 22.86%, respectively. Their favorable performance is attributed to suitable energy-band alignment, efficient hole extraction, balanced carrier transport, and reduced recombination under the investigated simulation conditions. The integrated analyses demonstrate that HTL selection governs device behavior primarily through interface-controlled electrical processes, while the sensitivity to the assumed defect conditions further influences carrier recombination and overall device performance. These findings provide a comprehensive physical understanding of HTL-controlled interface engineering in lead-free $RbSnBr_3$ perovskite solar cells and offer theoretical guidance for their future experimental optimization.

Keywords: Perovskites, Solar Energy, PCE, Fill Factor, Environmental Friendly

Introduction:

Large-scale industrialization and environmental degradation have raised the energy consumption rate of the world to a level that necessitates the demand of sustainable and renewable energy sources [1]. The high efficiency with which photovoltaic systems directly convert light into electrical energy using semiconducting materials has made them a preferred choice among renewable energy technologies. Solar energy is widely distributed across a larger geographical area unlike fossil fuel. It is renewable and in abundance that makes it a viable solution towards climate change and greenhouse gas emissions [2]. However, the limitations of the conventional photovoltaic (PV) technologies, particularly based on crystalline silicon, are their higher cost of production, rigid design of the modules and energy-intensive processing. These disadvantages limit their scalability and affordability [3]. Due to the higher Power Conversion Efficiencies (PCEs), the low processing cost and variable optoelectronic properties, Perovskite Solar Cells (PSCs) have emerged as the best choice for the third-generation photovoltaic devices. The Power Conversion Efficiency (PCE) of single-junction perovskite solar cells has rapidly increased to over 26% within a little more than a decade, demonstrating their remarkable potential for next-generation photovoltaic technologies [3]. Despite the rapid development and excessive research efforts being put in this field, the highest-performing PSCs are still produced with Pb-containing materials, specifically methylammonium lead iodide MAPbI3, which poses environmental and health concerns because of its toxicity and instability. These materials exhibit poor stability when exposed to moisture, oxygen and high temperatures which restricts their use in the long-term and makes it economically non-viable [4].

Inorganic perovskites without lead present a favorable solution. The tin (Sn) based perovskites are one possible solution because of similar optoelectronic properties as that of their lead-based counterparts and do not suffer from toxicity [5]. Meanwhile, $RbSnBr_3$ is lead-free and offers a suitable band gap, a high absorption coefficient, and the potential for improved environmental stability. Its environmental stability is expected to benefit from the absence of organic cations, although comprehensive experimental validation under long-term operating conditions is still required. $RbSnBr_3$ is a promising lead-free perovskite owing to its suitable bandgap, high absorption coefficient, and compatibility with solution-based fabrication. However, its long-term operational stability and large-area experimental realization still require further investigation [6].

The structure of the device used in this study is FTO/SnS_2/$RbSnBr_3$/HTLs/Au. The tin oxide (transparent anode) is fluorine doped (FTO) as it is an excellent conductor of electricity and optical transparency. The electron transport layer (ETL) is comprised of tin disulfide (SnS_2) which is an n-type semiconductor with a wide bandgap, chemical stability and good conduction band alignment [7]. SnS_2 was selected as the electron transport layer because of its wide bandgap, favourable conduction-band alignment with $RbSnBr_3$, high electron mobility, chemical stability, and compatibility with low-temperature processing, making it suitable for efficient electron extraction. $RbSnBr_3$ serves as the absorber layer, responsible for light absorption and electron-hole pair generation. [8].

In order to examine the importance of the hole transport layer (HTL) to device performance, five types of HTL materials are considered, including CuSCN, Cu2O, P3HT, PTAA and PEDOT:PSS. These HTLs provide different physical and electrical properties. An inorganic p-type semiconductor, CuSCN (Copper (I) thiocyanate) has a wide bandgap (3.6 eV) is highly optically transparent and has moderate hole mobility. It is a rhombohedral structured copper thiocyanate complex of ions and is thus well suited in inverted perovskite solar cells since it has highly chemical stability and because of its processability via solution cell processing. However, its energy levels should be properly aligned with the perovskite absorber

to prevent the occurrence of cliff-stalike offsets that are conducive to recombination [9]. Another naturally occurring inorganic HTL that has a cubic structure is Cu2O (Copper (I) oxide). It has p-type conductivity due to intrinsic copper vacancies and it has good hole mobility, chemical stability and non-toxicity. However, when coupled with the perovskites, it may have interfacial defects and lattice mismatch [10]. P3HT [Poly(3- hexylthiophene)] can be defined as a semi crystalline conjugated polymer, which consists of repeating units of thiophene featuring alkyl side chains, which allow 3-D stacking of 3-P pairs as well as moderate mobility of holes. It finds application in organic photovoltaic and is its hydrophobicity, flexibility and interfacial defect tolerance (although its hole mobility is lower than other advanced HTLs) [11]. PTAA (Poly [bis(4-phenyl)(2, 6-trimethylphenyl)amine]) is a high-performance polymer HTL, which has arylamine as its units that enable easy conduction of holes and a high glass transition temperature with superior thermal stability. It has already demonstrated a good performance in high efficiency PSCs, but its application is constrained by the fact that it is rather expensive and sensitive to processing conditions [12]. Lastly, a commonly used water-soluble conducting polymer complex is PEDOT:PSS (Poly(3,4-ethylenedioxythiophene):poly(styrene sulfonate)) in which PEDOT and PSS confer conductivity and uniformity of the films respectively. It has been widely employed because of its solution process ability, favorable energy-level alignment, and efficient hole extraction. However, its acidic and hygroscopic nature may adversely affect long-term device stability, making its performance highly dependent on interface engineering and encapsulation strategies [13][14].

The hole transport layer plays a critical role in determining interface energetics, carrier extraction, and recombination behaviour in perovskite solar cells. Appropriate HTL selection influences the open-circuit voltage, fill factor, and overall device efficiency through its energy-level alignment, carrier mobility, and interfacial defect characteristics. Therefore, systematic evaluation of different HTLs is essential for understanding interface-controlled device physics and optimizing lead-free perovskite solar cells. [15].

Despite these advantages, PEDOT:PSS also exhibits certain limitations. Its acidic and hygroscopic nature has been reported to accelerate electrode corrosion, moisture-assisted degradation, and interfacial losses during long-term device operation. To overcome these challenges, recent interface-engineering strategies, particularly self-assembled monolayers (SAMs) and buried-interface modification, have been proposed to suppress interfacial recombination, improve energy-level alignment, and enhance operational stability. Nevertheless, PEDOT:PSS remains one of the most extensively investigated HTLs owing to its excellent film-forming ability, high optical transparency, suitable work function, and compatibility with low-temperature solution processing. Therefore, PEDOT:PSS, together with other established polymeric HTLs such as P3HT, continues to serve as an important benchmark material for evaluating and comparing emerging hole transport layers in perovskite solar cells. [16]

The HTLs are all simulated using the SCAPS-1D simulation tool that is applied to the same device structure but numerically solving the drift diffusion equations of charge transport and recombination. The simulations are run under normal AM 1.5G light. [17] and investigate the impact of the choice of HTL on the most significant photovoltaic parameters, including open circuit voltage (VOC), short circuit current density (JSC), fill factor (FF) and total power conversion efficiency (PCE). Except for the HTL-specific material properties, all device parameters were kept identical to ensure a controlled comparison among the investigated HTLs. All material parameters were adopted from experimentally or theoretically validated literature sources and maintained consistently throughout the simulations to ensure a fair and reproducible comparison among the investigated HTLs.

Novelty Statement:

Although SCAPS-1D has been widely used to investigate transport-layer effects in perovskite solar cells, a systematic physical comparison of different HTLs specifically for lead-free $RbSnBr_3$ solar cells remains limited. The novelty of the present work lies in establishing a controlled HTL-dependent analysis within a fixed FTO/SnS_2/$RbSnBr_3$/HTL/Au device framework, where five representative inorganic and polymeric HTLs (CuSCN, Cu_2O, P3HT, PTAA, and PEDOT:PSS) are evaluated under identical absorber, ETL, contact, and operating conditions. This controlled framework enables the HTL-dependent contribution to device behaviour to be examined without changing the underlying device architecture or simulation conditions. More importantly, the study goes beyond a conventional comparison of power-conversion efficiency by establishing correlations among energy-band alignment, carrier transport, recombination, bulk and interface defect response, contact work function, and electrical characteristics to explain the origin of the different photovoltaic responses obtained with the investigated HTLs.[18]

A further contribution of this work is the integrated interpretation of these coupled HTL-dependent effects rather than treating individual parameter sweeps as independent sources of novelty. In particular, the band-alignment, recombination, defect-response, transport, and contact-engineering results are considered together to clarify why HTLs with apparently favorable behavior in one physical aspect do not necessarily produce the highest overall photovoltaic performance. The study therefore provides a physically connected interface-engineering framework for comparing HTLs in $RbSnBr_3$-based solar cells, identifying the interplay between interfacial energetics, carrier extraction, recombination, and transport that governs the simulated device response. This framework provides a basis for rational HTL selection in numerical $RbSnBr_3$ device design, while the conclusions remain subject to the assumptions and limitations of the SCAPS-1D model.[19]

Methodology:

The photovoltaic and electrical characteristics of the proposed lead-free perovskite solar cell were simulated using SCAPS-1D (version 3.3.12). This simulator is widely used for modelling multilayer thin-film solar cells and enables detailed investigation of photovoltaic and electrical characteristics, including the open-circuit voltage (V_{OC}), short-circuit current density (J_{SC}), fill factor (FF), power conversion efficiency (PCE), quantum efficiency (QE), and energy-band profiles. SCAPS-1D numerically solves Poisson's equation together with the electron and hole continuity equations under steady-state conditions [20].

$$\frac{\partial^2 \Psi}{\partial x^2} = -\frac{\partial E}{\partial x} = -\frac{\rho}{\varepsilon_x} = -\frac{\rho}{\varepsilon_x}\left[\mathrm{p} - \mathrm{n} + N_d^+ - N_a^- \pm N_{def}\right] \quad (1)$$

where Ψ represents electrostatic potential, ε_s represents relative permittivity, 'q' represents charge, 'n' represents electrons and 'p' represents holes. 'N_{d+}' represents donor density, 'Na ' represents acceptor density and 'N_{def}' represents donor/acceptor defect density. The continuity equations for holes and electrons are given below:

$$\frac{\partial_{j_P}}{\partial x} + G - U_P(n,p) = 0 \quad (2)$$

$$\frac{\partial_{j_n}}{\partial_x} + G - U_n(n,p) = 0 \quad (3)$$

The recombination rates of the holes and the electrons are represented by $U_p(n, p)$ and $U_n(n, p)$, respectively. G, J_p and J_n represent the symbols for the charge carrier generation rate, current density of the holes and the current density of the electrons, respectively. The carrier current density may be derived from these parameters:

$$j_p = qp\mu_p E - qD_p \frac{\partial p}{\partial x} \quad (4)$$

$$j_n = qn\mu_n E + qD_n \frac{\partial n}{\partial x} (5)$$

Here, the diffusion coefficients are termed D_p and D_n and the mobilities of the carriers are represented by μ_n and μ_p with the charge represented by q.

The solar cell was simulated under standard AM 1. 5G illumination, incident light intensity of 1000 W/m² and a temperature of 300 K, unless otherwise stated [21]. The SCAPS solver numerically solves Poisson's equation and electron and hole continuity equations, with drift diffusion, generation and recombination. The simulation considered both bulk defects and interfacial recombination sites, simulated with given energetic depth and capture cross sections. Shallow acceptor doping was introduced into the HTLs for p-type conductivity. Main electrical parameters such as VOC, JSC, FF and PCE were extracted, along with supporting diagnostics such as quantum efficiency (QE), C–V and G–V characteristics and energy band profiles. For the C–V and G–V calculations, an AC frequency of 1 MHz was used at 300 K. The C–V characteristics were evaluated over a bias range of 0–1.2 V with a voltage increment of 0.02 V. The simulations were performed under AM1.5G illumination with an incident light intensity of 1000 W/m², and the same conditions were applied to all investigated HTLs to ensure a consistent comparison. For the optical generation calculation, $RbSnBr_3$ was modelled using the SCAPS traditional $\sqrt{(h\nu - Eg)}$ absorption model with Eg = 1.28 eV. The model parameters were $\alpha_0 = 1.0 \times 10^5$ cm^{-1} and $\beta_0 = 1.0 \times 10^{-12}$, with the wavelength-dependent absorption coefficient calculated by SCAPS over 0.2–0.9787 μm using 101 mesh points. The resulting absorption-coefficient data used in the simulations are provided in the Supplementary Information. The absorber thickness was varied from 0.1 to 2.0 μm to investigate its influence on light absorption and carrier recombination. Similarly, the HTL and ETL (SnS_2) thicknesses were varied from 0.01–0.2 μm and 0.01–0.10 μm, respectively. Bulk defect density was varied from 10^{11} to 10^{16} cm^{-3}, whereas interface defect density was varied from 1010 to 1015 cm^{-2} to investigate the influence of recombination pathways on device performance [22]. The present study primarily focuses on Shockley–Read–Hall (SRH) recombination because trap-assisted recombination is generally considered the dominant loss mechanism in lead-free perovskite solar cells containing defect states under normal operating conditions. Radiative and Auger recombination were therefore not analysed separately in the present comparative SCAPS-1D study. Although these mechanisms may contribute under specific operating conditions, their quantitative investigation is beyond the scope of the present work and may be considered in future studies.

Simulation Workflow:

The numerical investigation was performed through a sequential simulation workflow using SCAPS-1D. First, the material parameters and layer properties of the device components were defined based on the literature values reported in Tables 1 and 2. Second, the baseline FTO/SnS_2/$RbSnBr_3$/HTL/Au device structure was established under AM1.5G illumination at 1000 W/m² and 300 K. Third, five HTLs, namely CuSCN, Cu_2O, P3HT, PTAA, and PEDOT:PSS, were incorporated into the same device architecture, while the absorber, SnS_2 ETL, metal contacts, illumination conditions, and numerical settings were kept unchanged. The J–V characteristics were then calculated to obtain VOC, JSC, FF, and PCE for comparative evaluation. Subsequently, the effects of absorber, HTL, and ETL thickness, bulk and interface defect density, carrier mobility, and contact work function were investigated through systematic parameter variations. Finally, the devices were further evaluated using QE, C–V/G–V characteristics, energy-band profiles, generation and recombination analysis, and temperature-dependent simulations. The results from these analyses were compared among the five HTLs to establish correlations between HTL-dependent material properties, carrier transport, recombination behaviour, interface response, and overall photovoltaic performance.

To ensure a fair and scientifically meaningful comparison, all device parameters, including the absorber layer, electron transport layer, metal contacts, illumination conditions, defect model, and numerical simulation settings, were kept identical throughout all simulations. Only the material properties of the HTLs were varied according to the corresponding literature values. Consequently, the observed variations in the simulated photovoltaic and electrical characteristics are interpreted as the combined influence of the different HTL properties, while the device architecture and simulation conditions are kept unchanged. The same interface-defect parameters were applied at both the SnS_2/$RbSnBr_3$ and $RbSnBr_3$/HTL interfaces for all investigated devices to ensure a consistent and reproducible comparison. Accordingly, the interface-defect analysis represents the sensitivity of the simulated devices to a common assumed defect model rather than intrinsic HTL-specific defect properties. In the present SCAPS-1D model, interface defects were implemented as interface-defect states; therefore, interface defect densities are expressed in cm^{-2}, whereas bulk defect densities are expressed in cm^{-3}. No finite-thickness interfacial defect layer was assumed in the simulations. SnS_2 was intentionally selected as the fixed electron transport layer because of its favourable conduction-band alignment with $RbSnBr_3$, high electron mobility, chemical stability, and previously demonstrated suitability for lead-free perovskite solar cells. This controlled simulation methodology enabled the evaluation of how HTL-dependent properties influence carrier extraction, recombination behaviour, sensitivity to the assumed defect conditions, and the resulting electrical characteristics under identical operating conditions. All material parameters, including layer thickness, bandgap, electron affinity, dielectric constant, carrier mobility, doping concentration, and defect parameters, were adopted from previously published experimental or validated SCAPS-based studies. The corresponding literature sources are provided in Tables 1 and Table 2 to ensure complete transparency, traceability, and reproducibility of the simulations.

Table 1. Material parameters of different ETL, HTLs and Absorber.

Parameters	Symbol	$RbSnBr_3$ [6]	SnS2 [8]	CuSCN [9]	Cu2O [10]	P3HT [11]	PTAA [23]	PEDOT :PSS [13]
Thickness	d (μ_m)	0.8	0.02	0.17	0.05	0.35	0.02	0.500
Bandgap	E_g (eV)	1.28	2.4	3.4	2.2	1.7	2.96	1.8
Electron Affinity	X (eV)	4	4.24	1.9	3.4	3.5	2.3	3.4
Relative Permittivity	ε_r	3.93	10	10	7.5	3	9	3
Conduction Band Density	N_c (cm^{-3})	$1.62x10^{19}$	$2.2x10^{18}$	$1.7x10^{19}$	$2x10^{19}$	$2x10^{18}$	$1x10^{21}$	$2.2x10^{18}$
Valence Band Density	N_v (cm^{-3})	$5.1x10^{18}$	$1.8x10^{19}$	$2.5x10^{21}$	$1x10^{19}$	$2x10^{18}$	$1x10^{21}$	$1.8x10^{19}$
Electron Thermal Velocity	V_e(cms^{-1}	$1x10^7$	$1x10^7$	$1x10^7$	$1x10^7$	$1x10^7$	$1x10^7$	$1x10^7$
Hole Thermal Velocity	V_h(cms^{-1}	$1x10^7$	$1x10^7$	$1x10^7$	$1x10^7$	$1x10^7$	$1x10^7$	$1x10^7$
Electron Mobility	μ_n (cm^2/Vs)	23.76	50	0.0001	200	$1.8x10^{-3}$	10	$1x10^2$
Hole Mobility	μ_p (cm^2/Vs)	50.23	50	0.1	8600	$1.8x10^{-2}$	40	4
Donor Concentration	N_D (cm^{-3})	$1x10^9$	$1x10^{16}$	0	$1x10^{15}$	0	0	0

Acceptor Concentration	N_A (cm^{-3})	$1x10^9$	0	$1x10^{18}$	0	$1x10^{19}$	$1x10^{19}$	$2x10^{19}$

Table 2. Bulk and interface defect parameters used in the SCAPS-1D simulations.

Parameter [24]	**Bulk Defect**	**SnS_2/$RbSnBr_3$ Interface**	**$RbSnBr_3$/HTL Interface**
Defect type	Neutral	Neutral	Neutral
Defect density (Nt)	10^{11}–10^{16} cm^{-3} (varied)	10^{11}–10^{16} cm^{-2} (varied)	10^{11}–10^{16} cm^{-2} (varied)
Energy distribution	Single	Single	Single
Defect energy level (Et)	0.60 eV above EV	0.60 eV above highest EV	0.60 eV above highest EV
Electron capture cross-section	1.0×10^{-15} cm^2	1.0×10^{-2} cm s^{-1} (left/right)	1.0×10^{-2} cm s^{-1} (left/right)
Hole capture cross-section	1.0×10^{-15} cm^2	1.0×10^{-2} cm s^{-1} (left/right)	1.0×10^{-2} cm s^{-1} (left/right)
Defect grading	Uniform	Uniform	Uniform

Table 3. Performance benchmark of the optimised HTL-engineered $RbSnBr_3$ perovskite solar cells against previously reported $RbSnBr_3$-based devices

Device Structure	**Voc (V)**	**Jsc (mA/cm^2)**	**FF (%)**	**PCE (%)**	**Ref**
FTO/SnS_2/$RbSnBr_3$/CuSCN/Au	0.9141	33.616678	73.47	22.58	This Study
FTO/SnS_2/$RbSnBr_3$/Cu_2O/Au	0.9141	33.623077	69.84	21.46	This Study
FTO/SnS_2/$RbSnBr_3$/P3HT/Au	0.9161	33.672055	74.11	22.86	This Study
FTO/SnS_2/$RbSnBr_3$/PTAA/Au	0.9141	33.616729	73.52	22.59	This Study
FTO/SnS_2/$RbSnBr_3$/PEDOT:PSS/Au	0.9158	33.712157	74.08	22.87	This Study
FTO/TiO_2/$RbSnBr_3$/PTAA/Au	0.78	35.05	73.06	22.53	[6]
ITO/WS_2/$RbSnBr_3$	0.89	47.14	78.92	33.25	[7]
FTO/SnS_2/$RbSnBr_3$	0.98	47.21	77.67	29.79	[7]

For reproducibility, the SCAPS-1D input parameters were explicitly specified for each simulated layer, including the bandgap, electron affinity, relative permittivity, carrier mobility, doping concentration, layer thickness, and defect-related parameters. The front and back contact work functions, illumination conditions, operating temperature, and interface-defect assumptions were also kept explicitly defined. The numerical values and their corresponding literature sources are provided in Tables 1 and 2, while the simulation workflow and sequence of the performed analyses are illustrated in Figure 3. These details allow the investigated device configurations and parameter-variation procedures to be reproduced using the same SCAPS-1D version and boundary conditions.

Device Modelling and Analysis:

Device modelling was performed using the SCAPS-1D simulator, which numerically solves Poisson's equation together with the electron and hole continuity equations under steady-state conditions. The simulator was employed to investigate the performance of the proposed single-junction FTO/SnS_2/$RbSnBr_3$/HTL/Au device by systematically analysing how different hole transport layers (HTLs) influence interface energetics, charge transport, recombination behaviour, sensitivity to defect conditions, electrical characteristics, and overall photovoltaic performance under identical simulation conditions [25].

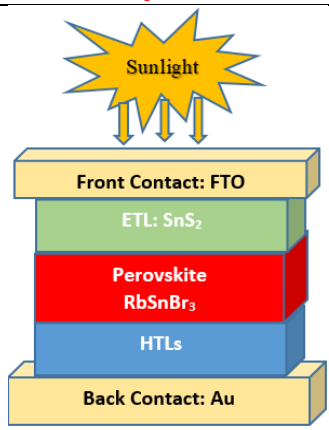


Figure 1. Device Structure of the $RbSnBr_3$ Perovskite Solar Cell

The simulated device consists of a planar FTO/SnS_2/$RbSnBr_3$/HTL/Au architecture, in which SnS_2 serves as the electron transport layer (ETL), $RbSnBr_3$ acts as the light-absorbing layer, and five representative inorganic and polymeric HTLs (CuSCN, Cu_2O, P3HT, PTAA, and PEDOT:PSS) were evaluated. Figure 1 illustrates the device architecture, while Figure 2 presents the comparative energy-band alignment of all investigated HTLs. The conduction band minimum (CBM) and valence band maximum (VBM) of each layer were estimated from the electron affinity and bandgap values listed in Table 1 to provide a comparative assessment of the nominal HTL/absorber band alignment. This diagram represents the static band-edge alignment derived from the adopted material parameters and does not include equilibrium band bending, quasi-Fermi-level splitting, or bias-dependent operating-condition profiles.

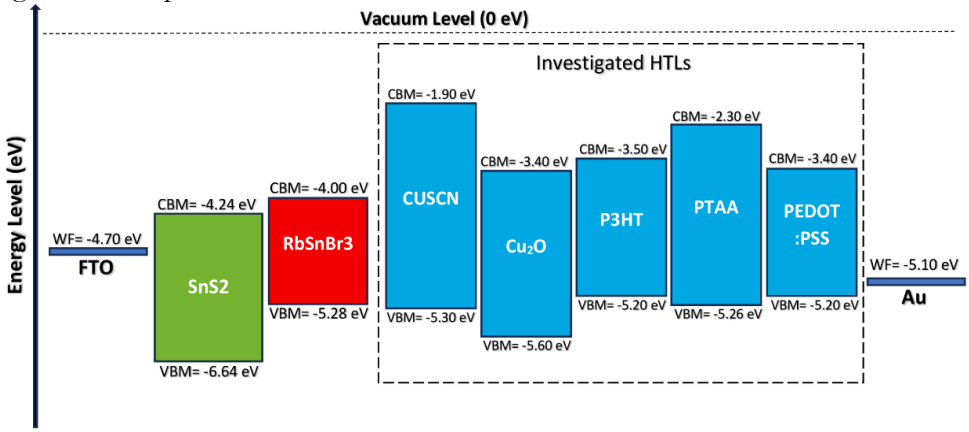


Figure 2. Comparative energy-band alignment of the investigated HTLs with the FTO/SnS_2/$RbSnBr_3$ device.

To ensure a controlled and physically meaningful comparison, only the HTL material was varied, whereas the absorber, ETL, contacts, illumination conditions, defect model, and all numerical simulation parameters were kept identical throughout the study. This approach enables a controlled evaluation of the combined influence of HTL properties on the simulated device behaviour while the absorber, ETL, contacts, illumination conditions, and numerical settings are kept unchanged.

Each material layer was modelled using experimentally or theoretically reported physical parameters, including bandgap, electron affinity, dielectric constant, carrier mobility, doping concentration, and defect density, as summarised in Table 1. Because the investigated HTLs differ simultaneously in their intrinsic electronic, transport, dielectric, doping, density-of-states, and thickness parameters, the present comparison is interpreted as a combined HTL-property assessment rather than as an independent sensitivity analysis of any single material

parameter. The bulk and interface defect models were defined using the defect type, energetic distribution, defect energy level, and electron and hole capture cross-sections, as summarised in Table 2. Furthermore, the effects of carrier mobility, bulk and interface defect density, contact work function, absorber thickness, series resistance (Rs), shunt resistance (Rsh), capacitance–voltage (C–V), conductance–voltage (G–V), and temperature-dependent operation were evaluated to examine the sensitivity of the simulated device response to these parameters. The overall SCAPS-1D simulation workflow is illustrated in Figure 3.

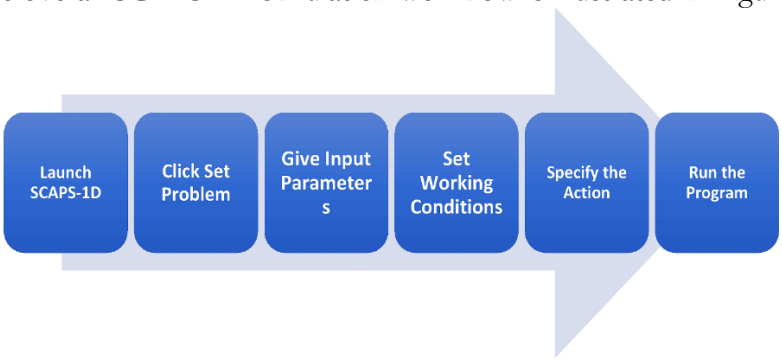


Figure 3. Stepwise Working Mechanism of SCAPS-1D Simulator

Result and Discussion:

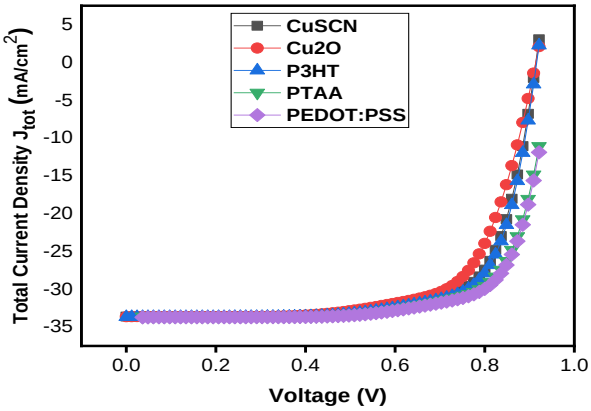


Figure 4. J–V Characteristics of $RbSnBr_3$ Solar Cell with Different HTLs

Figure 4 illustrates the J-V characteristics of the devices having various HTLs and all devices have almost the same short circuit current density (J_{SC}= 33.6-33.7mA/cm^2) hence the nearly flat region of the J-V curve at the negative current indicates that the photogeneration in the $RbSnBr_3$ absorber is efficient and is not dependent on the choice of HTL [26]. These disparities seem to be close to the open circuit voltage scale i.e. the curves of PEDOT:PSS and P3HT keep going along the voltage axis than the curves of Cu2O and CuSCN. This indicates that the polymer-based HTLs provide more favourable band alignment with the perovskite valence band, resulting in reduced recombination and improved charge extraction. Consequently, PEDOT:PSS and P3HT exhibit nearly identical J-V characteristics, with simulated PCEs of 22.87% and 22.86%, respectively. The negligible performance difference indicates that both polymer-based HTLs provide similarly favourable interfacial energetics, efficient hole extraction, and reduced recombination under the investigated simulation conditions. In comparison, the curve of Cu2O and CuSCN shifts earlier to zero current, indicating a higher interfacial loss and, therefore, lower VOC and FF. These trends affirm that the curvilinear nature of the JV curve close to VOC is dictated by the quality of interfaces and band matching that finally makes the difference between high and poor HTLs. These observations demonstrate that the differences in device performance originate primarily from HTL-dependent interface properties rather than from changes in optical generation. Because all devices employ the same absorber, ETL, contacts, and operating conditions, the observed

variations can be interpreted in terms of the combined differences in HTL energy-level alignment, hole extraction, transport, and interface recombination. This controlled comparison establishes a clear relationship between interface energetics, carrier transport, and photovoltaic performance, providing physical insight into how HTL selection governs the electrical behaviour of $RbSnBr_3$-based perovskite solar cells. The results are in line with previous studies on polymer perovskite interfaces showing that a better interfacial charge dynamic, namely, the minimization of recombination and maximization of hole extraction, have a direct effect on the open circuit voltage and overall device performance. As an additional consistency check, the present simulation results were compared with an independently reported SCAPS-1D study of $RbSnBr_3$-based solar cells. The reported device achieved a PCE of 22.53%, JSC of 35.05 mA/cm², VOC of 0.87 V, and FF of 73.06%, whereas the present optimized PEDOT:PSS device achieved 22.87%, 33.71 mA/cm², 0.92 V, and 74.08%, respectively. The close agreement in the simulated photovoltaic parameters provides an independent consistency check of the present modelling approach, while the remaining differences can be attributed to the different device architecture, transport layers, and adopted material parameters.

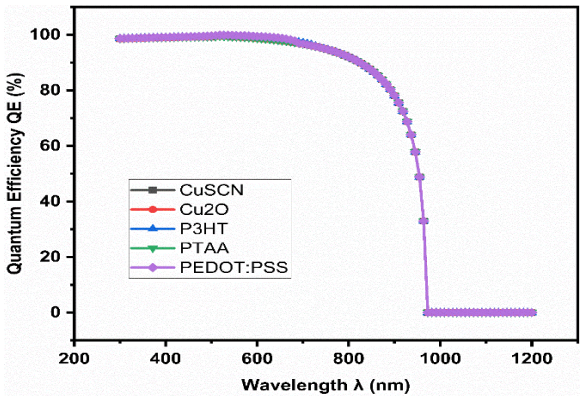


Figure 5. Quantum Efficiency (QE) Spectra of Devices with Varying HTLs

Figure 5 indicates that the Quantum Efficiency (QE) spectra of all devices are nearly the same with the use of various HTLs [27]. The simulated QE remains above 90% from 0.3 to 0.818 μm under the optical assumptions adopted in the SCAPS-1D model. All HTLs exhibit nearly identical QE spectra, with only marginal differences in the peak QE values (99.47–99.86%). All devices exhibit a simulated QE plateau above 98% throughout the 0.4–0.8 μm range, indicating efficient charge collection within the SCAPS-1D modelling framework. However, beyond 0.964 μm, the efficiency for all devices drops sharply toward zero as the incident photon energy falls below the absorber's bandgap. Since the optical absorption and carrier generation are governed primarily by the $RbSnBr_3$ absorber rather than the HTLs, and because the absorber band gap, optical constants, and thickness remain unchanged in all simulations, the carrier-generation profile remains essentially unchanged. These simulated results suggest that the QE spectra are primarily governed by the optical properties of the $RbSnBr_3$ absorber, whereas the HTL has only a limited influence on the simulated spectral response and mainly affects the electrical characteristics of the device. Therefore, the comparable QE spectra indicate that the optical generation profile is primarily determined by the $RbSnBr_3$ absorber, whereas the performance differences among the investigated HTLs arise predominantly from their influence on interface-assisted carrier extraction and recombination. This distinction confirms that HTL optimisation mainly modifies the electrical response of the device rather than its optical absorption.

To further verify the consistency of the simulated QE response, the QE spectra were numerically integrated with the AM1.5G reference spectrum to obtain the corresponding

photocurrent density. The resulting QE-derived J_{SC} values were 33.93, 33.93, 33.99, 33.93, and 34.03 mA/cm² for CuSCN, Cu_2O, P3HT, PTAA, and PEDOT:PSS, respectively. These values are in close agreement with the J_{SC} values obtained from the simulated J–V characteristics (approximately 33.6–33.7 mA/cm²), with differences of less than approximately 1%. This agreement provides a consistency check between the simulated spectral response and the photovoltaic current obtained from the J–V characteristics.

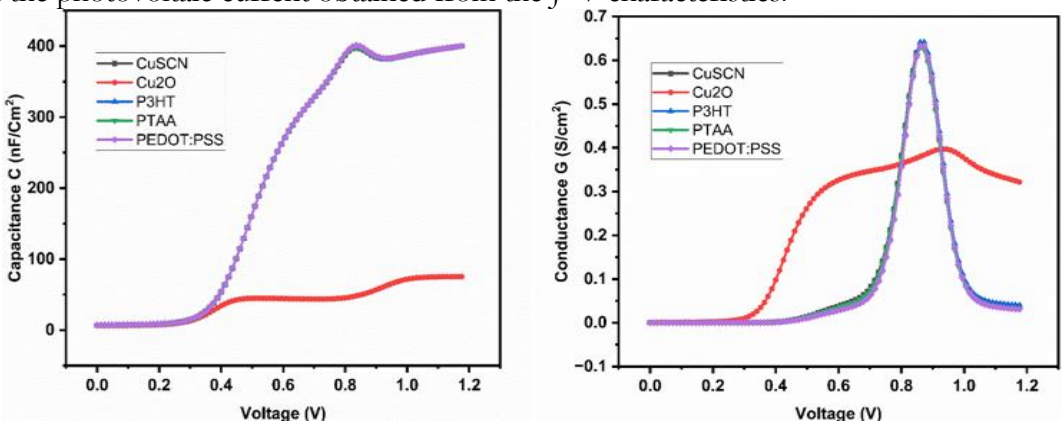
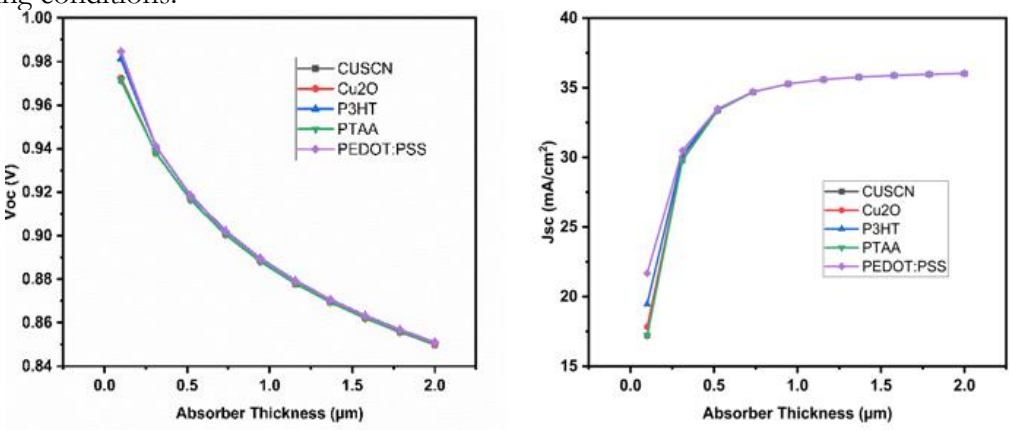


Figure 6. Capacitance–Voltage (C–V) and Conductance–Voltage (G–V) Characteristics

The C–V and G–V plots of the investigated devices are presented in Figure 6. Polymer HTLs (P3HT and PEDOT:PSS) show higher capacitance at zero bias (approximately 7 nF/cm²) than the inorganic HTLs Cu_2O and CuSCN (approximately 6.3 and 6.6 nF/cm², respectively). Consequently, the polymer-based devices exhibit higher initial capacitance under the adopted simulation conditions. With increasing bias, the capacitance gradually increases and approaches a saturation value of approximately 400 nF/cm² [28]. The G–V response also differs among the HTLs: Cu_2O exhibits a more pronounced conductance response, with a peak of approximately 0.40 S/cm², whereas the polymer HTLs show comparatively flatter conductance curves. These differences indicate that the investigated HTLs produce different simulated capacitive and conductance responses under the adopted AC conditions. However, the C–V and G–V results are interpreted here as comparative electrical-response characteristics and are not taken as standalone evidence of interfacial polarisation, enhanced charge storage, smoother hole extraction, or improved recombination blocking. The C–V and G–V characteristics therefore complement the J–V analysis by demonstrating that the choice of HTL affects the simulated electrical response of the device under otherwise identical modelling conditions.



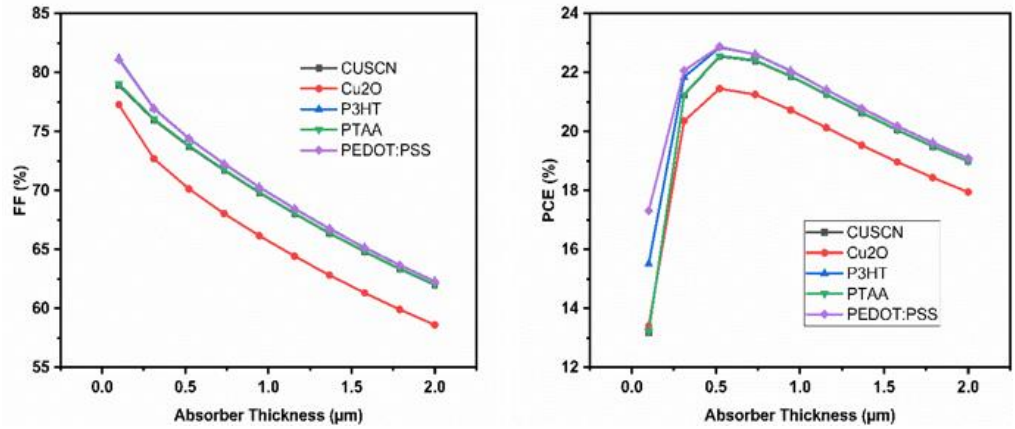
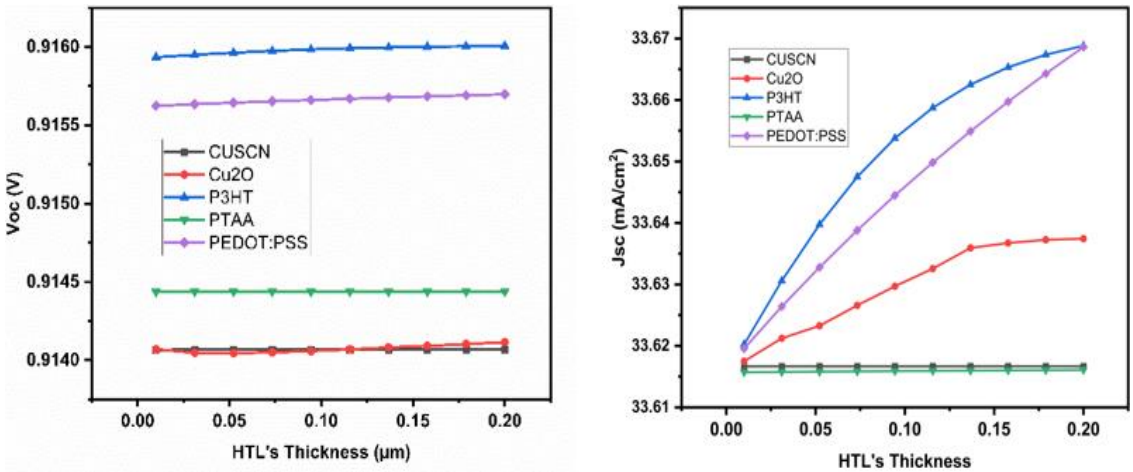


Figure 7. Effect of Absorber Layer Thickness on Device Electrical Parameters (Voc, Jsc, FF, PCE)

The influence of absorber thickness on the performance of the device is presented in Figure 7 [29]. As the absorber thickness increases from 0.1 to 2 μm, all devices show a consistent increase in JSC from a range of 17.21–21.67 mA/cm² to approximately 36.02 mA/cm², corresponding to an increase of approximately 14.35–18.81 mA/cm² depending on the HTL. This increase is consistent with enhanced optical absorption and a larger photogeneration volume at greater absorber thickness. Conversely, VOC gradually decreases, indicating that the additional absorber thickness does not translate into a proportional electrical gain and is accompanied by increased recombination losses. At increased thicknesses, the fill factor also decreases because thicker absorber layers increase carrier transport losses and recombination, thereby reducing charge-collection efficiency. The power conversion efficiency reaches its optimum at an absorber thickness of approximately 0.52 μm, where PEDOT:PSS and P3HT exhibit nearly identical simulated performances (22.87% and 22.86%, respectively), with an absolute difference of only 0.01 percentage points (0.04% relative). This optimum thickness therefore represents a balance between enhanced optical absorption and increasing carrier recombination/transport losses. Beyond this thickness, the additional increase in J_{SC} becomes progressively limited, while recombination and transport losses continue to increase, resulting in performance saturation. These results further indicate that although absorber thickness directly governs the optical generation volume, the final device performance remains influenced by HTL-dependent interface properties that determine the efficiency with which the generated carriers are extracted. Thus, the thickness-dependent response provides quantitative evidence that increasing absorber thickness primarily improves current generation up to an optimum point, after which electrical losses offset the optical benefit.



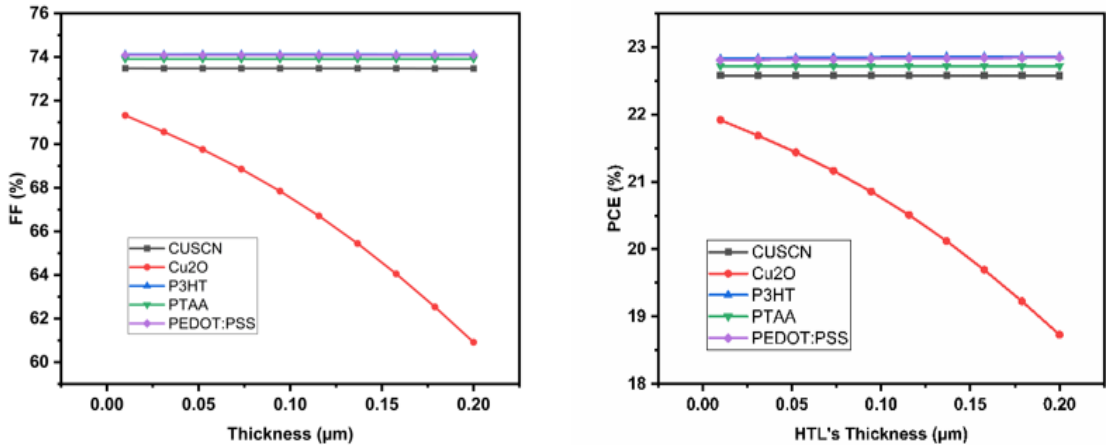
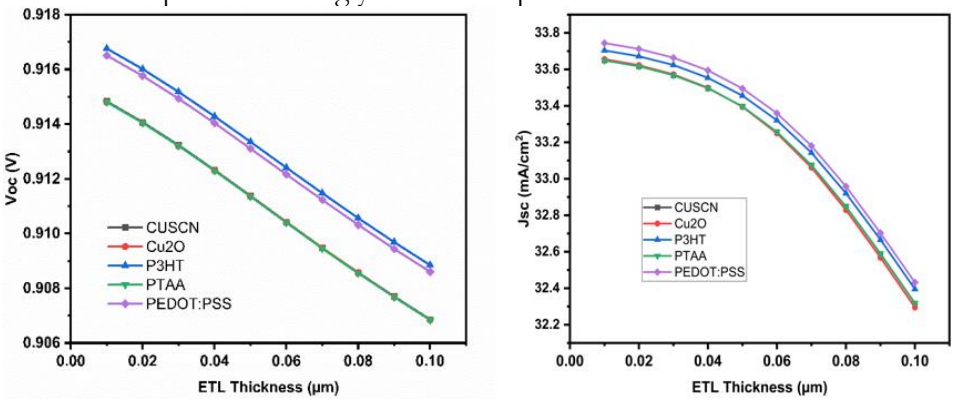


Figure 8. Influence of HTL Thickness Variation on Device Electrical Parameters (Voc, Jsc, FF, PCE)

Figure 8 compares the impact of HTL thickness on the photovoltaic parameters. As the HTL thickness increases from 0.01 μm to 0.2 μm, the photovoltaic parameters for most devices remain relatively stable, except for Cu_2O. Across all HTLs, J_{SC} shows only a marginal increase, remaining within 33.62–33.67 mA/cm², corresponding to a total variation of approximately 0.05 mA/cm² (0.15%). Meanwhile, V_{OC} remains nearly constant at approximately 0.91 V, indicating that the change in HTL thickness has little influence on the photogeneration-related current or the open-circuit voltage under the adopted conditions. However, the FF for Cu_2O drops significantly from 71.32% to 60.92%, representing a reduction of 10.40 percentage points (14.6% relative), which leads to a corresponding decline in its PCE from 21.92% to 18.73%, a reduction of 3.19 percentage points (14.6%). In contrast, other materials such as P3HT and PEDOT:PSS maintain high stability, with PCE values slightly improving or remaining approximately 22.86%. The polymer-based HTLs therefore show substantially smaller performance variation over the investigated thickness range than Cu_2O. The strong Cu_2O-specific reduction in FF and PCE, despite the nearly unchanged J_{SC} and V_{OC}, indicates that the thickness effect is primarily associated with electrical transport losses rather than changes in optical generation. These trends suggest that increasing HTL thickness can modify carrier transport resistance and recombination behaviour, particularly for the oxide-based HTL. The greater thickness tolerance observed for the polymeric HTLs further demonstrates that their simulated photovoltaic performance remains comparatively insensitive to HTL thickness over the investigated range. These findings indicate that HTL thickness primarily affects the electrical characteristics of the device through changes in carrier transport resistance and interface recombination rather than through optical effects, while the magnitude of the response is strongly material-dependent.



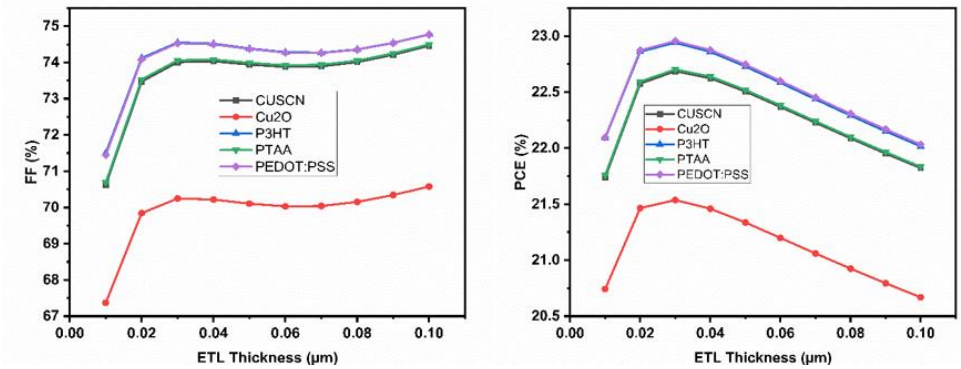
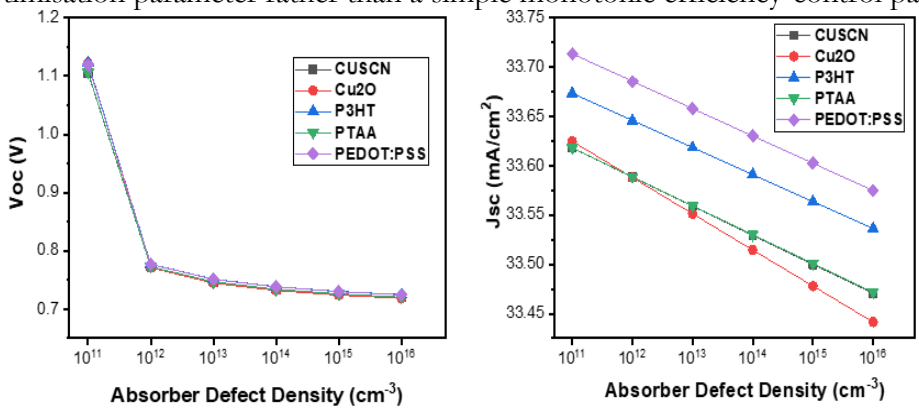


Figure 9. Effect of ETL (SnS_2) Thickness Variation on Device Electrical Parameters (Voc, Jsc, FF, PCE)

Figure 9 analyses the impact of SnS_2 (ETL) thickness on the performance of the device. As the ETL thickness increases from 0.01 μm to 0.1 μm, J_{SC} across all devices gradually decreases from 33.70 mA/cm² to 32.40 mA/cm², corresponding to a reduction of 1.30 mA/cm² (3.9%). V_{OC} shows a comparatively small reduction from 0.916 V to 0.908 V, corresponding to only 0.008 V (0.9%). In contrast, the FF improves for all HTLs, rising from a range of 67.37–71.50% to 70.58–74.78%, corresponding to an improvement of approximately 3.21–7.41 percentage points depending on the HTL. These opposing changes indicate that increasing ETL thickness simultaneously influences current extraction and the fill-factor-related electrical losses. Due to these competing trends, the PCE remains relatively stable, peaking around 0.03 μm and reaching 22.95% for PEDOT:PSS before experiencing a minor decline at higher thicknesses. Beyond this thickness, device performance decreases slightly because the thicker ETL introduces additional carrier transport resistance, reducing charge-extraction efficiency. The relatively small change in V_{OC} compared with the 3.9% reduction in J_{SC} suggests that the dominant thickness-dependent effect in this range is associated with electron transport and extraction rather than a substantial change in the built-in voltage. These findings are in agreement with previous numerical research that determined an optimal ETL thickness range of 0.03–0.04 μm in order to extract charge effectively in perovskite solar cells [30]. These observations confirm that the ETL mainly controls electron extraction and transport, whereas the relative differences among the investigated devices continue to be governed by the HTL/perovskite interface. Maintaining the same ETL for all simulations therefore enables the influence of HTL properties on device behaviour to be isolated without interference from variations in electron transport. Overall, the relatively narrow PCE variation around the optimum ETL thickness, together with the simultaneous decrease in J_{SC} and increase in FF, demonstrates that ETL thickness represents a transport-related optimisation parameter rather than a simple monotonic efficiency-control parameter.



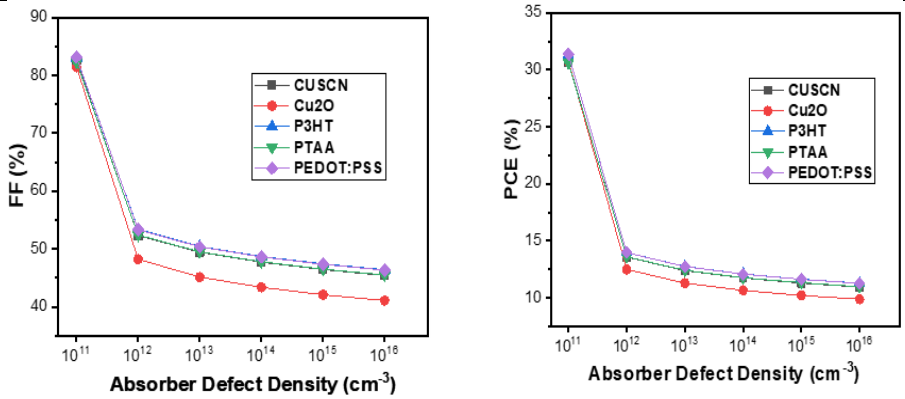


Figure 10. Effect of Absorber Defect Density on Device Electrical Parameters (Voc, Jsc, FF, PCE)

Figure 10 shows the influence of absorber defect density on the photovoltaic characteristics. As the absorber defect density increases from 10^{11} to 10^{16} cm^{-3}, J_{SC} remains relatively stable, decreasing only slightly from 33.72 to 33.45 mA/cm², corresponding to a change of approximately 0.8%. In contrast, V_{OC} decreases substantially from 1.12 to 0.72 V, corresponding to a reduction of approximately 35.7%, while FF decreases from approximately 83% to 42%, corresponding to a reduction of approximately 49.4%. Consequently, the PCE decreases from a peak value of approximately 31.39% to around 10%, representing a reduction of approximately 68.1%. The peak PCE of approximately 31.39% obtained at the lowest absorber defect density should not be interpreted as the baseline device efficiency. This value corresponds to the absorber defect-density sensitivity analysis under the reduced bulk-defect condition, whereas the baseline PCE of 22.87% corresponds to the standard device parameter set used for the main HTL comparison. The difference therefore arises from the change in absorber bulk-defect density and does not represent an inconsistency in the baseline device performance. The comparatively small change in J_{SC} , despite the large reductions in V_{OC} , FF, and PCE, indicates that increasing defect density primarily affects carrier recombination and voltage/transport losses rather than the optical generation of carriers. Among the investigated HTLs, PEDOT:PSS and P3HT maintain comparatively higher efficiencies at increased defect densities, indicating lower sensitivity to defect-induced recombination under the simulated conditions. The negligible difference between these two polymer HTLs indicates comparable sensitivity to bulk-defect density within the investigated range. In contrast, CuSCN and Cu_2O exhibit the steepest performance losses. The findings are consistent with previous literature showing that defect passivation and absorber/interface quality are important for maintaining the performance of lead-free perovskite devices [31]. The strong decrease in VOC and FF relative to the small variation in JSC provides quantitative evidence that bulk defects predominantly introduce non-radiative recombination and carrier-transport losses rather than substantially modifying photogeneration. These results demonstrate that bulk-defect optimisation alone is insufficient to maintain high device performance. The response of each device to increasing defect density is also governed by the HTL/$RbSnBr_3$ interface, which determines how efficiently photogenerated carriers are extracted before trap-assisted recombination occurs. Therefore, the combined analysis of bulk-defect density and HTL selection provides deeper insight into defect tolerance and interface-controlled recombination than photovoltaic parameters alone.

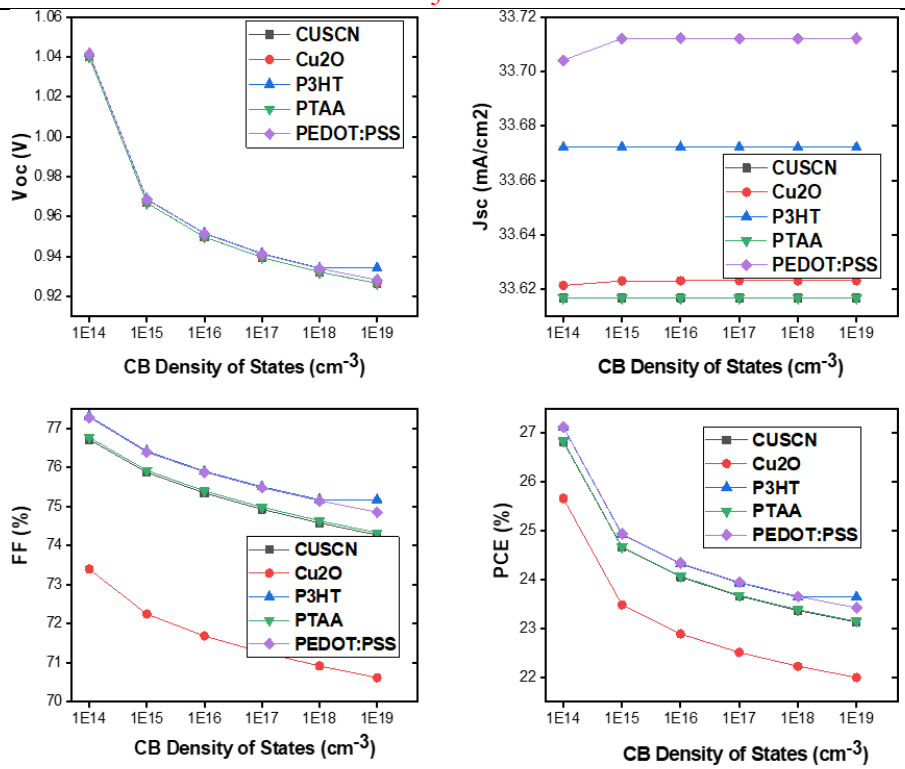


Figure 11. Impact of Absorber Conduction Band Density of States on Device Electrical Parameters (Voc, Jsc, FF, PCE)

Figure 11 demonstrates the influence of conduction-band (CB) density of states (DOS) in the absorber on the performance of the devices. As the CB-DOS increases from 10^{14} to 10^{19} cm^{-3}, J_{SC} across all devices remains nearly constant at approximately 33.60–33.71 mA/cm^2, indicating a change of less than approximately 0.3% over the investigated range. In contrast, V_{OC} decreases from 1.04 to 0.93 V, corresponding to a reduction of approximately 10.6%, while the FF decreases from approximately 77% to 74% for most HTLs; for Cu_2O, the FF decreases from 73.5% to 70.5%. Consequently, the PCE for all HTLs except Cu_2O decreases from a maximum of 27.13% to approximately 23.65%, corresponding to a reduction of approximately 12.80%. PEDOT:PSS and P3HT maintain comparable simulated efficiencies, indicating similar sensitivity to CB-DOS variation under the investigated conditions, whereas CuSCN and Cu_2O exhibit comparatively stronger responses to changes in DOS [32]. The substantially smaller variation in JSC compared with VOC and PCE indicates that the increased CB-DOS primarily modifies the electronic-state distribution associated with carrier recombination and voltage losses rather than the photogeneration process. These results are corroborated by previous simulations reporting that conduction-band tail states can limit V_{OC} in perovskite devices and that polymer-based HTLs may exhibit lower sensitivity to CB-DOS variation under comparable simulation conditions. The increased density of conduction-band states provides additional electronic states that can influence carrier recombination and transport. By maintaining identical absorber properties and varying only the HTL, the present analysis distinguishes the influence of HTL-dependent interface energetics from the intrinsic sensitivity of the absorber electronic structure. Thus, the quantitative changes in V_{OC} , FF, and PCE, despite the nearly unchanged J_{SC} , provide additional evidence that CB-DOS mainly affects the electrical and recombination characteristics of the device rather than its optical generation.

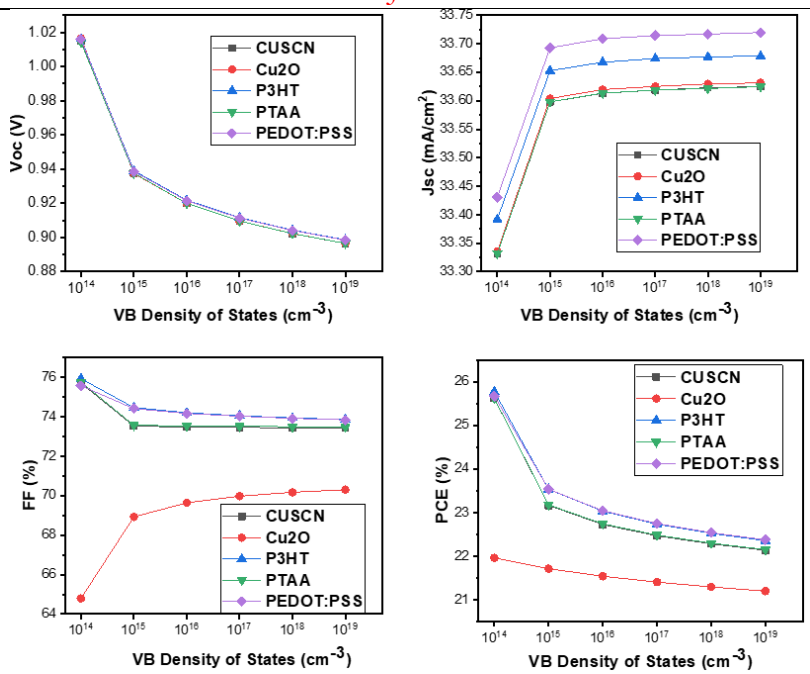


Figure 12. Impact of Absorber Valence Band Density of States on Device Electrical Parameters (Voc, Jsc, FF, PCE)

Figure 12 examines how an increase in valence-band (VB) density of states (DOS) affects the performance of the devices [33]. As the VB-DOS increases from 1014 to 1019 cm−3, JSC across all devices shows a slight improvement, rising from 33.33 to 33.72 mA/cm², corresponding to an increase of approximately 1.2%. In contrast, V_{OC} decreases from 1.02 to 0.90 V, representing a reduction of approximately 11.8%, while the FF decreases from approximately 76% to 74%, corresponding to a reduction of approximately 2.6%, except for Cu_2O, for which the FF increases from 64.1% to 70%. Consequently, the PCE for all HTLs decreases from a peak value of 25.77% to approximately 22.37%, corresponding to a reduction of approximately 13.2%. PEDOT:PSS and P3HT maintain nearly identical simulated efficiencies throughout the investigated VB-DOS range. The comparatively small change in J_{SC} , together with the larger reduction in V_{OC} , indicates that increasing VB-DOS primarily influences voltage losses and recombination-related electrical behaviour rather than the optical generation of carriers. These findings indicate that polymer-based HTLs maintain comparatively higher photovoltaic performance under increased VB-DOS conditions, in line with previous studies reporting the influence of HTL/absorber alignment on the V_{OC} of perovskite devices. The results further demonstrate that HTL selection influences the electrical response through carrier extraction and recombination processes at the interface rather than through optical generation alone. The combined VB-DOS and HTL analysis therefore provides additional quantitative insight into the interaction between absorber electronic states and interface engineering, while the similar response of PEDOT:PSS and P3HT indicates that their relative advantage is maintained over the investigated VB-DOS range rather than arising from a single DOS value.

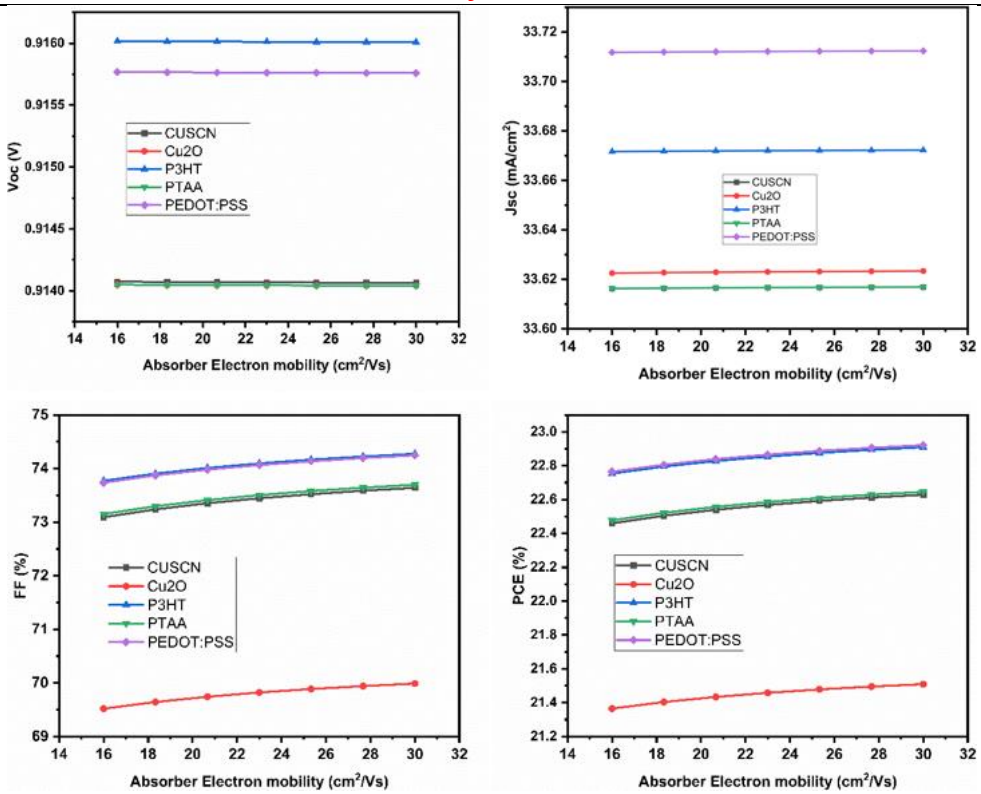


Figure 13. Effect of Electron Mobility on Device Electrical Parameters (Voc, Jsc, FF, PCE)

Figure 13 illustrates the effect of absorber electron mobility on the photovoltaic performance of the investigated devices. As the absorber electron mobility increases from 16 to 30 cm^2/Vs, V_{OC} and J_{SC} remain almost constant across all HTLs, with V_{OC} at approximately 0.91 V and J_{SC} at 33.6–33.7 mA/cm^2, indicating that the investigated mobility range has little influence on photogeneration or the open-circuit voltage under the adopted simulation conditions. In contrast, a measurable improvement is observed in the fill factor, which increases from 69.52–73.77% at 16 cm^2/Vs to 69.99–74.27% at 30 cm^2/Vs, corresponding to an increase of approximately 0.50–0.68 percentage points depending on the HTL. Consequently, the PCE also increases for all devices, with PEDOT:PSS and P3HT reaching nearly identical simulated efficiencies of approximately 22.92% and 22.91%, respectively. The relatively small change in PCE despite an almost twofold increase in electron mobility indicates that the devices are not strongly transport-limited by absorber electron mobility within the investigated range. Instead, once sufficient electron transport is available, further mobility enhancement produces only a limited improvement in the overall photovoltaic response. This interpretation is consistent with the observed stability of V_{OC} and J_{SC} and the comparatively modest change in FF. The results therefore suggest that increasing electron mobility primarily reduces transport-related losses and improves charge extraction, while its influence on recombination is comparatively limited under the simulated conditions, as found in other previous works on transport-limited perovskite devices [34]. This also demonstrates that improvements in bulk transport parameters alone cannot fully optimise device performance without favourable HTL/$RbSnBr_3$ interfacial properties.

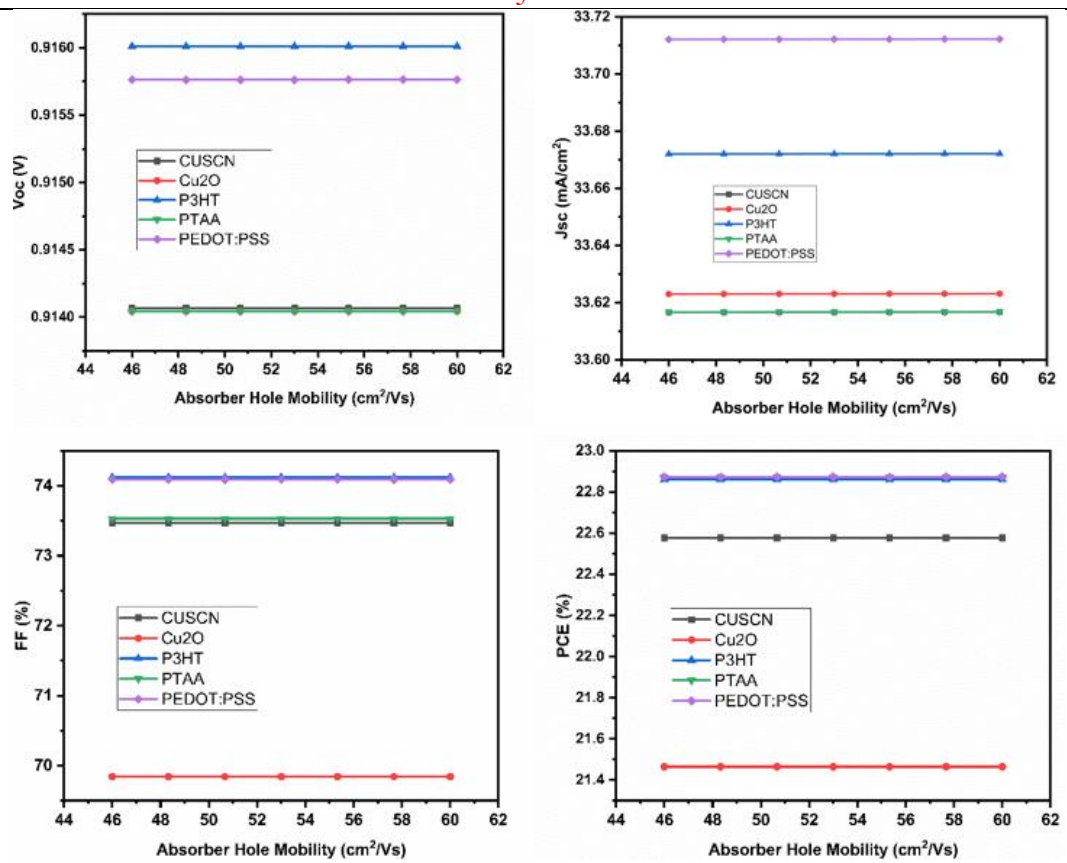


Figure 14. Effect of Hole Mobility on Device Electrical Parameters (Voc, Jsc, FF, PCE)

Figure 14 illustrates the effect of absorber hole mobility on device performance. As the absorber hole mobility increases from 46 to 60 cm^2/Vs, all photovoltaic parameters, including V_{OC}, J_{SC}, FF, and PCE, remain almost entirely constant across all HTLs. Specifically, V_{OC} remains at approximately 0.91 V, while J_{SC} remains within 33.6–33.7 mA/cm^2 and FF varies between 69.84% and 74.12% over the investigated mobility range. Consequently, the PCE values show negligible change, with PEDOT:PSS and P3HT continuing to exhibit nearly identical simulated efficiencies of approximately 22.87%. The limited variation in the photovoltaic parameters despite an increase of approximately 30% in absorber hole mobility indicates that hole transport is already sufficiently efficient within the investigated range and that further mobility enhancement does not substantially reduce the dominant device losses. These findings suggest that an increase in hole mobility plays a minor role in efficiency by reducing resistive losses, as other past studies have shown that mobility gains alone cannot radically improve performance unless they are accompanied by optimisation of interfacial properties. Thus, increasing hole mobility has only a minor influence on the simulated photovoltaic performance within the investigated range. These results indicate that once sufficient hole mobility is achieved within the absorber, further mobility enhancement contributes only marginally to device performance. Instead, the HTL/$RbSnBr_3$ interface remains an important factor governing carrier extraction and recombination, as also reflected by the larger sensitivity observed in the band-alignment and defect analyses. This observation further supports the conclusion that interface engineering, rather than bulk mobility optimisation alone, contributes substantially to the simulated performance.

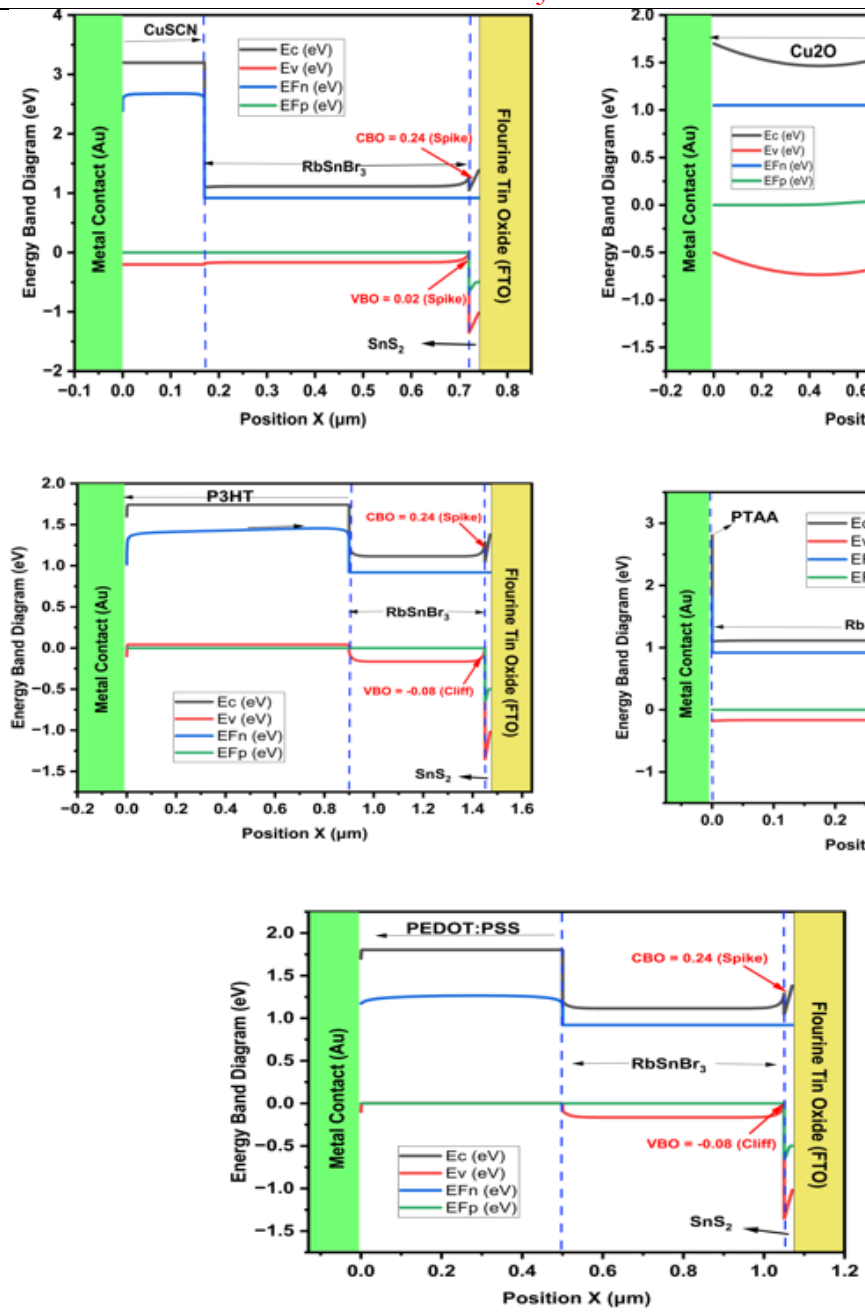


Figure 15. Nominal Energy-Band Alignment of Different HTLs

The band alignments of the various HTLs with the RbSnBr3 absorber are compared in Figure 15 [35]. The HTLs employed in this study possess different band-gap values, as listed in Table 1 (CuSCN = 3.4eV, Cu_2O = 2.2eV, P3HT = 1.7eV, PTAA = 2.96eV, and PEDOT = 1.8eV). Therefore, the device performance is governed by the relative conduction and valence band alignment at the HTL/absorber interface rather than by a common HTL band gap. Numerical analysis of the valence band alignment at the HTL/absorber interface reveals that the inorganic HTLs, CuSCN and Cu_2O, exhibit positive valence band offsets (VBOs) of +0.02 eV and +0.32 eV, respectively, creating spike-like alignments that can impede hole extraction. In contrast, the organic HTLs PTAA, P3HT, and PEDOT exhibit VBOs of −0.02 eV, −0.08 eV, and approximately 0.00 eV, respectively, providing more favourable interfacial energetics for efficient hole extraction. Given that some of these VBO differences are relatively small, particularly for CuSCN, PTAA, P3HT, and PEDOT:PSS, they should be

interpreted with caution because uncertainties in the adopted literature-derived material parameters may affect the exact offset values. These nominal valence-band offsets indicate potentially more or less favourable energetic alignment for hole extraction; however, they should not be considered as standalone evidence that the VBO alone governs hole extraction, interface recombination, or the resulting electrical behaviour. The band-alignment results are therefore considered together with the subsequent electrical and defect analyses to provide a comparative physical interpretation of HTL-dependent device behaviour rather than simply comparing photovoltaic efficiencies. These band-alignment differences provide one important contribution to the observed HTL-dependent behaviour; however, the resulting photovoltaic performance should be interpreted as the combined outcome of the HTL electronic and transport properties rather than as the consequence of a single interface parameter.

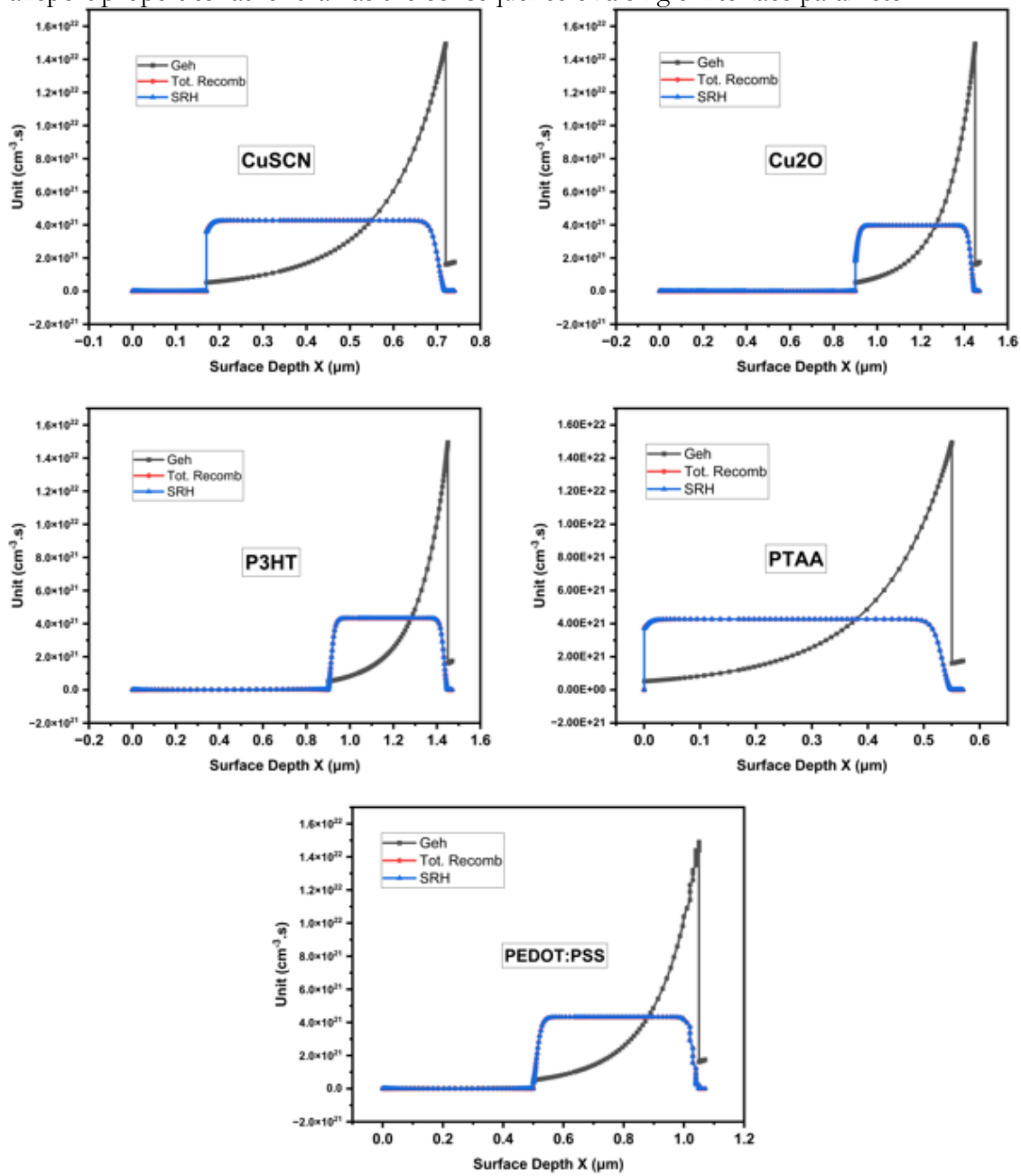


Figure 16. Generation and Recombination Profiles Across Device Depth for Various HTLs

Based on the generation and recombination profiles across the device depth shown in Figure 16, all five devices exhibit a similar peak carrier-generation rate of approximately 1.49 × 10^{22} cm^{-3} s^{-1}, confirming that the optical generation profile is essentially unchanged by the choice of HTL. The total recombination is predominantly governed by Shockley–Read–Hall (SRH) processes under the adopted simulation conditions. To complement the local peak values, the SRH recombination profiles were spatially integrated over the ETL, $RbSnBr_3$ absorber, and HTL regions. The resulting total integrated SRH recombination rates are 2.25 × 10^{17}, 2.07 × 10^{17}, 2.22 × 10^{17}, 2.25 × 10^{17}, and 2.22 × 10^{17} cm^{-2} s^{-1} for CuSCN, Cu_2O, P3HT, PTAA, and PEDOT:PSS, respectively. The $RbSnBr_3$ absorber accounts for the dominant contribution, approximately 78–81% of the total integrated SRH recombination, while the HTL contributes approximately 19% and the ETL contribution is comparatively negligible. Cu_2O therefore exhibits the lowest integrated SRH recombination, but this does not translate into the highest photovoltaic efficiency. PEDOT:PSS and P3HT instead provide the most favourable balance among energy-level alignment, carrier extraction, transport, and recombination, resulting in simulated PCEs of 22.87% and 22.86%, respectively. These results demonstrate that the photovoltaic response cannot be interpreted from a single local or integrated recombination metric in isolation [36].

The significance of the present analysis therefore lies in correlating the existing SCAPS outputs rather than treating each parameter sweep as an independent optimisation objective. The band-alignment results in Figure 15, recombination behaviour in Figure 16, defect-density response in Figure 20, and contact-engineering results in Figures 18 and 19 collectively show that HTL-dependent interface properties influence the electrical response through several coupled processes. Thus, the parameter variations investigated in this study are used to examine the sensitivity of the same physical device to different operating and material conditions, while the main physical interpretation is derived from their combined relationship with HTL-dependent interface energetics and charge extraction.

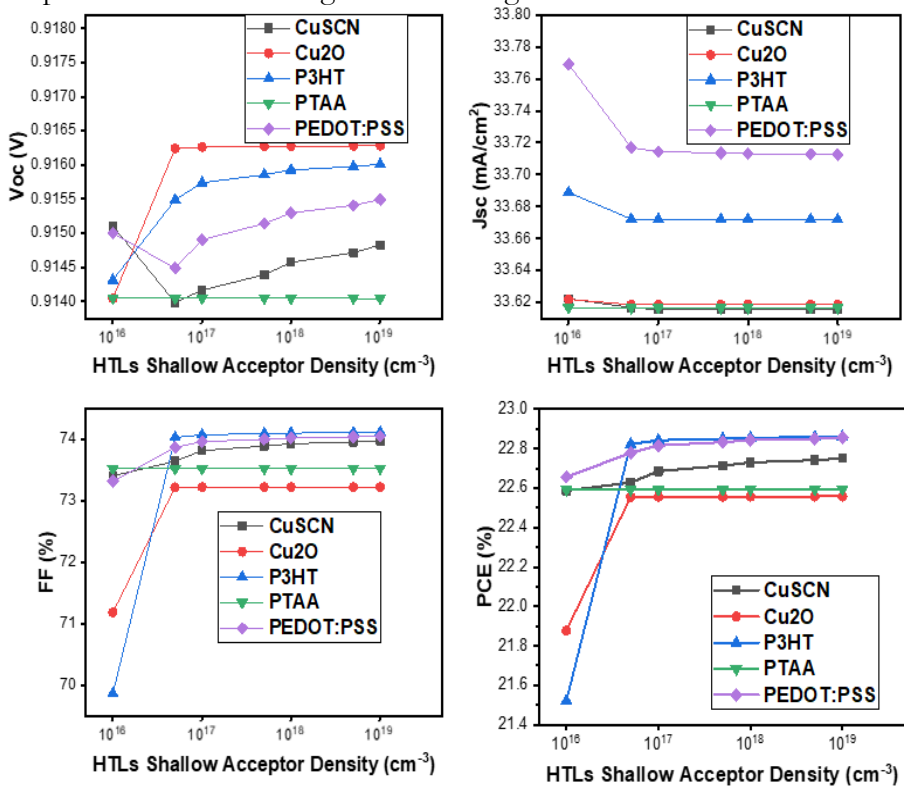


Figure 17. Effect of Shallow Acceptor Density in HTLs on Device Electrical Parameters (Voc, Jsc, FF, PCE)

Figure 17 shows how shallow acceptor density in various HTLs affects the performance of the devices. As it increases from 10^{16} to 10^{19} cm^{-3}, V_{OC} and J_{SC} remain relatively stable across all devices, with V_{OC} staying near 0.91 V and J_{SC} around 33.6–33.8 mA/cm^2, indicating that HTL acceptor doping has little influence on photogeneration and open-circuit voltage within the investigated range. The most notable improvement is observed in the FF, particularly for P3HT and Cu_2O, which increases from approximately 70% to above 74%, corresponding to an improvement of more than 4 percentage points. Consequently, the PCE for all HTLs shows a steady increase, reaching nearly identical simulated efficiencies of approximately 22.86–22.87% at higher doping levels. The convergence of the PCE values indicates that increasing the HTL acceptor density improves the electrical transport conditions but does not create a substantial difference between the investigated HTLs once sufficient conductivity is established. These results are consistent with previous research indicating that controlled HTL doping can enhance carrier transport and fill factor, while having no significant effect on V_{OC}. The simultaneous stability of V_{OC} and J_{SC} and the comparatively larger change in FF indicate that the primary effect of HTL doping in the present simulations is associated with transport resistance and hole extraction rather than optical generation or voltage generation. These results indicate that HTL doping primarily modifies the electrical conductivity of the transport layer and improves hole extraction without substantially affecting photogeneration or the built-in potential. Consequently, HTL optimisation requires simultaneous consideration of doping, energy-level alignment, and interface quality rather than doping concentration alone.

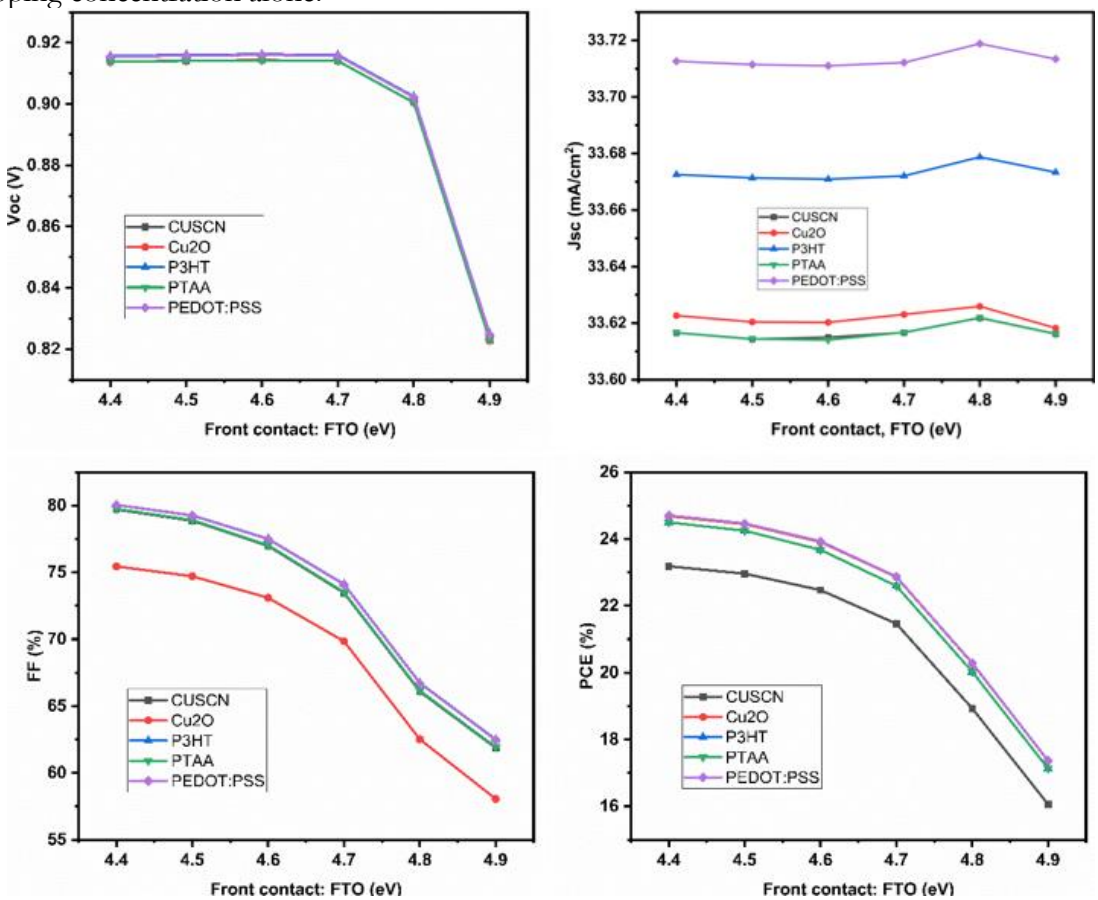


Figure 18. Influence of Front Contact (FTO) Work Function on Device Electrical Parameters (Voc, Jsc, FF, PCE)

Figure 18 assesses how the FTO work function affects the performance of the devices. As the work function increases from 4.4 to 4.9 eV, J_{SC} remains nearly constant at 33.6–33.7

mA/cm² across all devices, showing a variation of only approximately 0.1 mA/cm². In contrast, both V_{OC} and FF experience a significant decline, with V_{OC} dropping from 0.91 V to 0.82 V, corresponding to a voltage loss of approximately 0.09 V, while FF falls from 75.45–80.05% to 58.06–62.50%, representing a maximum reduction of approximately 17.55 percentage points. Consequently, the PCE for all HTLs decreases substantially from a peak range of 23.18–24.70% to 16.06–17.37%, corresponding to a reduction of approximately 27–35% relative to the respective higher values. PEDOT:PSS exhibits the highest simulated value; however, its overall behaviour remains very similar to that of P3HT across the investigated work-function range at 4.4 eV. Hence, PEDOT:PSS and Cu_2O maintain comparatively higher simulated efficiencies throughout the investigated work-function range, meaning that they are more compatible at the interface with the front electrode [37]. The much smaller change in J_{SC} compared with the pronounced changes in V_{OC}, FF, and PCE provides quantitative evidence that the FTO work function primarily affects the electrical/contact characteristics rather than the photogeneration process. These findings suggest that front-contact engineering primarily influences energy-level alignment and charge extraction, while having only a minor effect on J_{SC} under the simulated conditions, which agrees with additional reports of contact HTL interfacial optimisation of perovskite solar cells. These results demonstrate that front-contact work-function optimisation directly influences band alignment at the FTO/ETL interface, thereby affecting built-in potential, carrier extraction, and voltage loss. Together with the HTL optimisation presented throughout this work, these findings confirm that efficient device operation depends on coordinated interface engineering at both the front and rear contacts rather than optimisation of an individual layer alone.

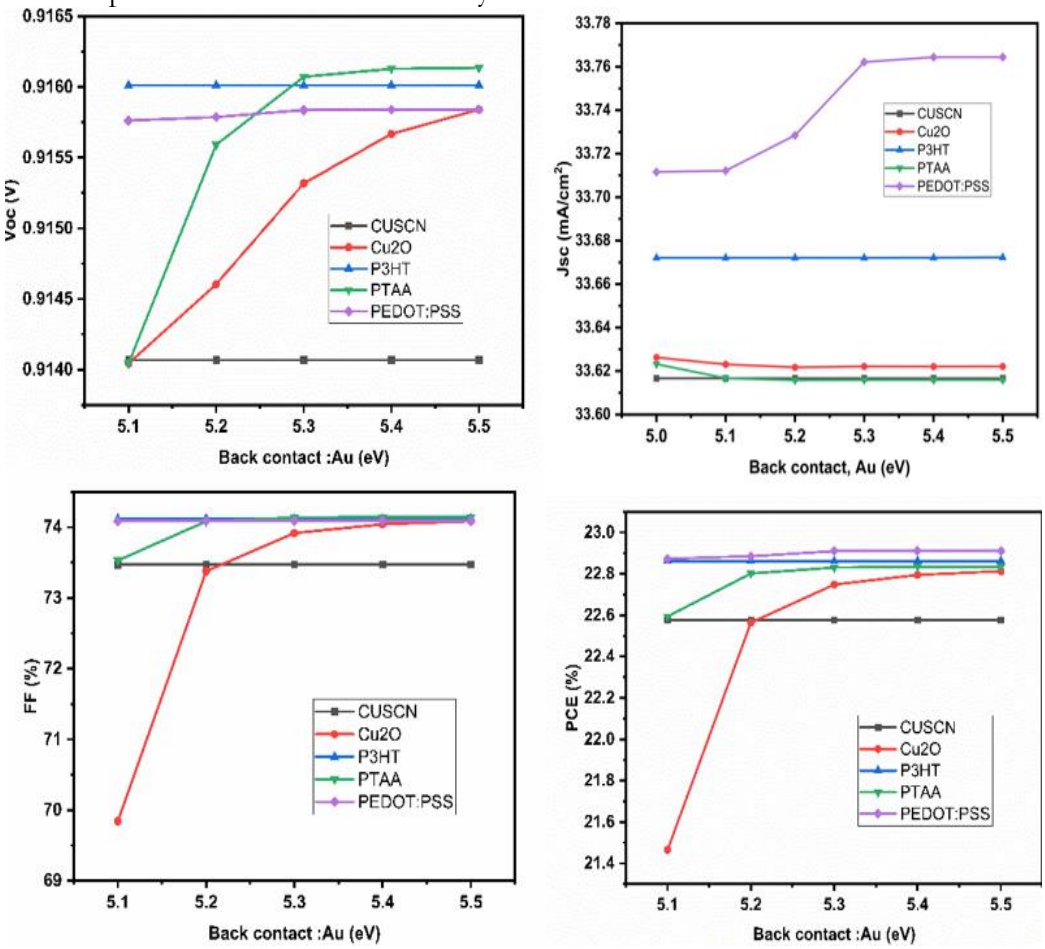


Figure 19. Influence of Back Contact (Au) Work Function on Device Electrical Parameters (Voc, Jsc, FF, PCE)

Figure 19 demonstrates the influence of different work functions of the Au back contact on the performance of the devices. As the work function increases from 5.0 to 5.5 eV, V_{OC} and J_{SC} remain mostly stable across all HTLs, with V_{OC} around 0.916 V and J_{SC} near 33.6–33.7 mA/cm². The most significant change occurs in the FF for Cu_2O, which improves remarkably from 61.14% to 74.09%, corresponding to an increase of approximately 12.95 percentage points. This change causes its PCE to rise from 18.81% to 22.81%, representing an improvement of approximately 21.3% relative to its initial value. For the other materials, the photovoltaic parameters remain comparatively high and steady, with PEDOT:PSS maintaining one of the highest simulated efficiencies at approximately 22.91%. The strong FF response of Cu_2O, despite the nearly unchanged V_{OC} and J_{SC}, indicates that the principal influence of the Au work function in this case is associated with contact-related carrier extraction and resistive losses rather than photogeneration or the absorber voltage response. These findings underscore the significance of back-contact engineering to reduce interfacial impediments and exploit as much as possible fill factor, in line with previous findings that underscore the importance of high-work-function metals in extracting holes in perovskite devices efficiently [38]. These results demonstrate that optimisation of the back-contact work function improves the electrical coupling between the HTL and the Au electrode, thereby reducing contact losses and enhancing carrier extraction. This further confirms that interface engineering at both the absorber/HTL and HTL/back-contact interfaces collectively governs the overall electrical performance of the device.

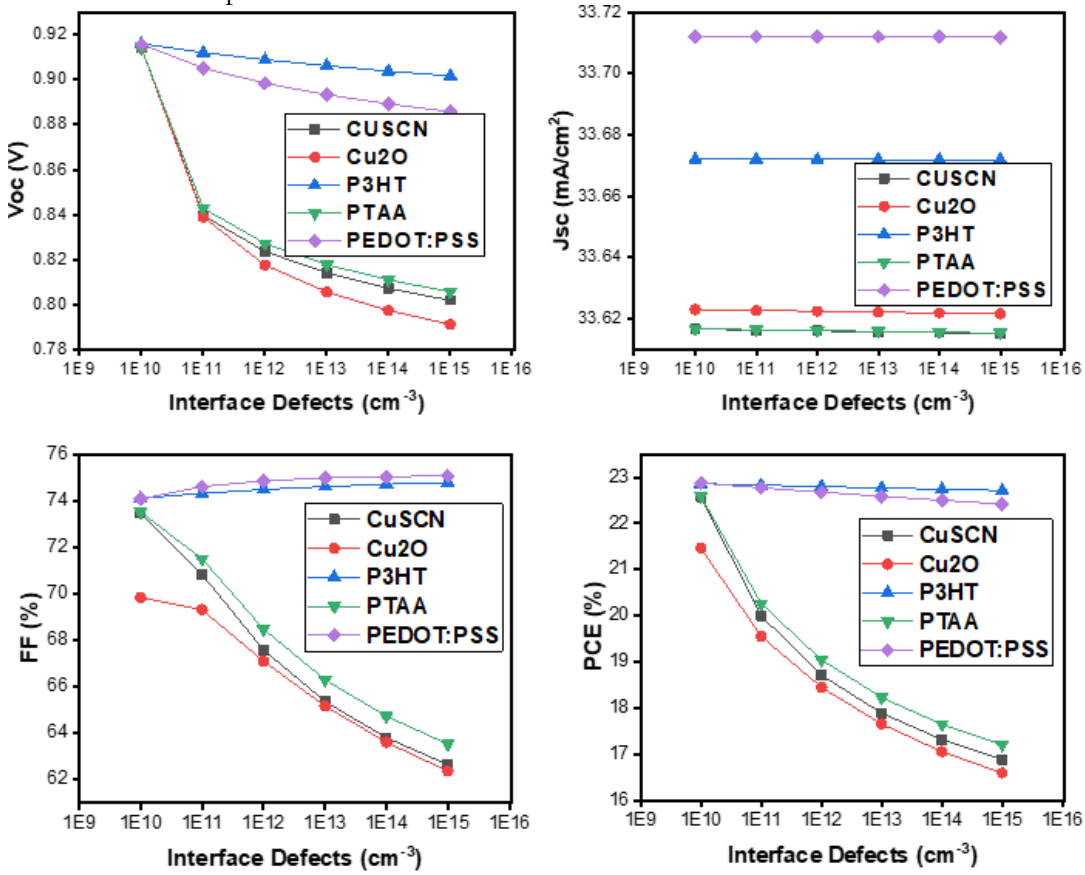


Figure 20. Impact of Interface Defect Density on Device Electrical Parameters (Voc, Jsc, FF, PCE) for Different HTLs

Figure 20 shows the sensitivity of the device performance to increasing interface-defect density under the common defect model adopted for all HTLs. As the interface defect density increases from 10^{10} to 10^{15} cm^{-2}, J_{SC} across all devices remains almost constant at

approximately 33.6–33.7 mA/cm², indicating that the assumed interface-defect variation has little effect on the photogeneration-related current under the adopted simulation conditions. However, a pronounced change is observed in V_{OC}, which decreases from 0.91 V to values as low as 0.79 V, corresponding to a maximum voltage loss of approximately 0.12 V, except for P3HT and PEDOT:PSS, for which V_{OC} remains approximately 0.9 V over the investigated range. FF also drops significantly for CuSCN, Cu_2O and PTAA, falling from approximately 73% to 62%, corresponding to a reduction of about 11 percentage points. Notably, P3HT and PEDOT:PSS show lower sensitivity to increasing interface-defect density under the simulated conditions, maintaining their FF and keeping their PCE above 22.4%, while the other HTLs experience a substantial efficiency reduction to approximately 16.6%. Thus, the difference between the relatively insensitive polymer devices and the more strongly affected HTLs becomes increasingly evident at high interface-defect densities. These findings support the fact that optimisation of interfacial traps is a key factor in attaining comparatively high efficiencies, in line with previous research highlighting the susceptibility of lead-free perovskites to interface quality. The simultaneous reduction in V_{OC} and FF, while J_{SC} remains nearly unchanged, is consistent with the role of interface defects as non-radiative recombination centres and carrier-extraction loss sites within the SCAPS model. The lower sensitivity of PEDOT:PSS and P3HT to increasing interface-defect density indicates that favourable interface energetics can partially mitigate the electrical losses associated with trap-assisted recombination under identical simulation conditions. This establishes a quantitative relationship between interface-defect density and HTL-dependent device behaviour. Because identical interface-defect parameters were assigned to all $RbSnBr_3$/HTL interfaces, these results should be interpreted as a comparative sensitivity analysis under a common assumed interface-defect model rather than as evidence of intrinsic HTL-specific defect tolerance.

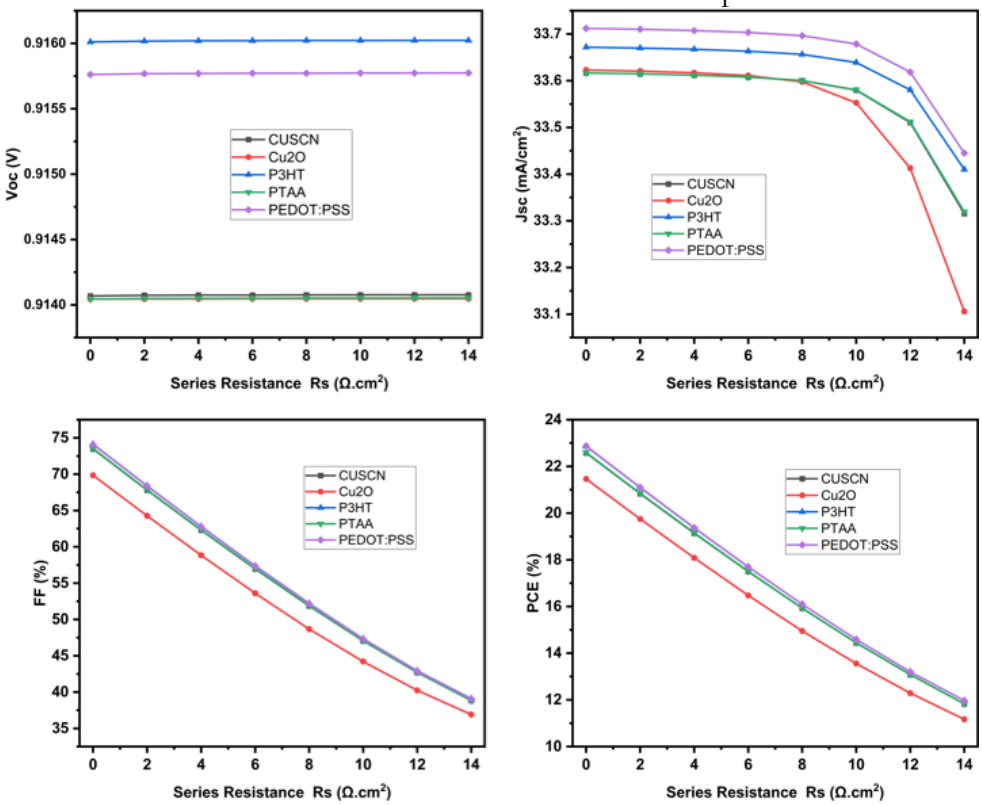


Figure 21. Effect of Series Resistance on Device Electrical Parameters (V_{OC}, J_{SC}, FF, PCE)

Figure 21 shows the dependence of the fill factor and power conversion efficiency on series resistance (Rs), with Rs variation having a significant influence on the electrical

performance of the device [39]. There is only a slight variation in VOC with increasing series resistance between 0 and 14 Ω.cm², remaining approximately 0.914 V. Similarly, J_{SC} shows only a small decrease, from 33.616 to approximately 33.59 mA/cm², corresponding to a change of only about 0.026 mA/cm². This indicates that photogeneration and the short-circuit current are comparatively insensitive to the imposed Rs variation. In contrast, the fill factor shows a pronounced degradation with increasing Rs, decreasing from approximately 73.47% at 0 Ω.cm² to 51.85% at 8 Ω.cm², corresponding to a reduction of approximately 21.62 percentage points. As a result, PCE is also substantially reduced; the efficiency of the P3HT-based device decreases to approximately 16.09%, also that of PEDOT:PSS decreases to approximately 16.09% under the corresponding high-resistance condition. The strong FF response compared with the negligible changes in V_{OC} and J_{SC} provides quantitative evidence that Rs primarily affects the resistive component of carrier extraction and the shape of the J–V characteristic near the maximum-power point. This trend can be attributed to the introduction of additional resistive losses into the carrier-transport pathway, thereby reducing the effective current flow through the device and altering the J–V characteristics near the power optimum. Consequently, FF and the overall efficiency are negatively affected, whereas V_{OC} and J_{SC} remain comparatively insensitive. These results indicate that series resistance mainly influences carrier transport after photogeneration by increasing resistive losses during charge extraction. Consequently, FF and PCE are strongly affected, whereas J_{SC} and V_{OC} remain comparatively insensitive. This demonstrates that transport resistance is another important electrical loss parameter associated with the charge-extraction pathway governing the overall device performance.

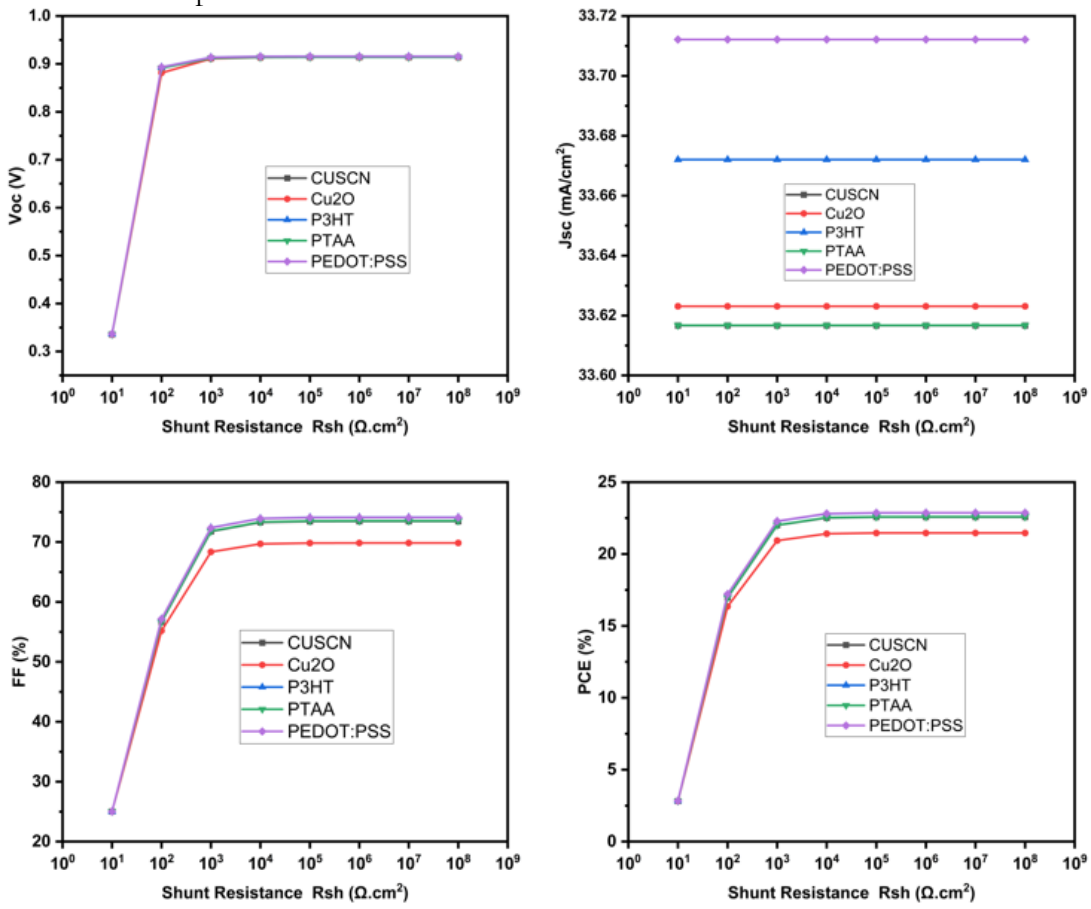


Figure 22. Effect of Shunt Resistances on Device Electrical Parameters (V_{OC}, J_{SC}, FF, PCE)

Figure 22 illustrates the effect of shunt resistance (R_{sh}) on device performance, which exhibits a trend opposite to that of the series resistance [40]. As the value of Rsh is varied from

10 to 10^5 Ω.cm², substantial changes occur in the voltage, fill factor, and efficiency. At Rsh = 10 Ω.cm², VOC is reduced significantly to approximately 0.336 V, compared with approximately 0.914 V at high Rsh, corresponding to a voltage recovery of about 0.578 V. This behaviour indicates that strong leakage-current pathways substantially limit the simulated voltage response at low shunt resistance. An increase in R_{sh} to 10^3 Ω.cm² causes V_{OC} to increase rapidly to approximately 0.912 V, after which it becomes relatively insensitive and stabilises around 0.914 V at higher values. Conversely, J_{SC} does not vary significantly throughout the range and remains close to 33.62 mA/cm², indicating that the photocarrier-generation process in the absorber is mostly independent of shunt resistance. The strongest changes are observed in FF and PCE. At R_{sh} = 10 Ω.cm², FF is only approximately 25%, and the PCE is very low, with efficiencies of 2.83% for P3HT and 2.84% for PEDOT:PSS. Increasing R_{sh} to 10^3 Ω.cm² raises the FF to approximately 71.76% and the PCE to approximately 22.28%, while at higher values in the range of 10^4–10^5 Ω.cm², FF reaches approximately 73.45% and PCE approximately 22.86%. Thus, increasing R_{sh} from 10 to 10^3 Ω.cm² produces an efficiency improvement of approximately 19.45 percentage points for P3HT, illustrating the strong impact of leakage losses at low R_{sh}. These observations demonstrate that shunt resistance primarily governs leakage-current pathways within the device. Increasing R_{sh} suppresses parasitic leakage and improves the effective carrier collection, thereby enhancing FF and PCE. The contrasting sensitivity of FF and PCE to R_{sh}, compared with the relatively stable J_{SC}, further supports the interpretation that shunt losses primarily affect the electrical extraction characteristics rather than optical generation. This further confirms that electrical losses associated with interface and contact quality significantly influence overall device performance.

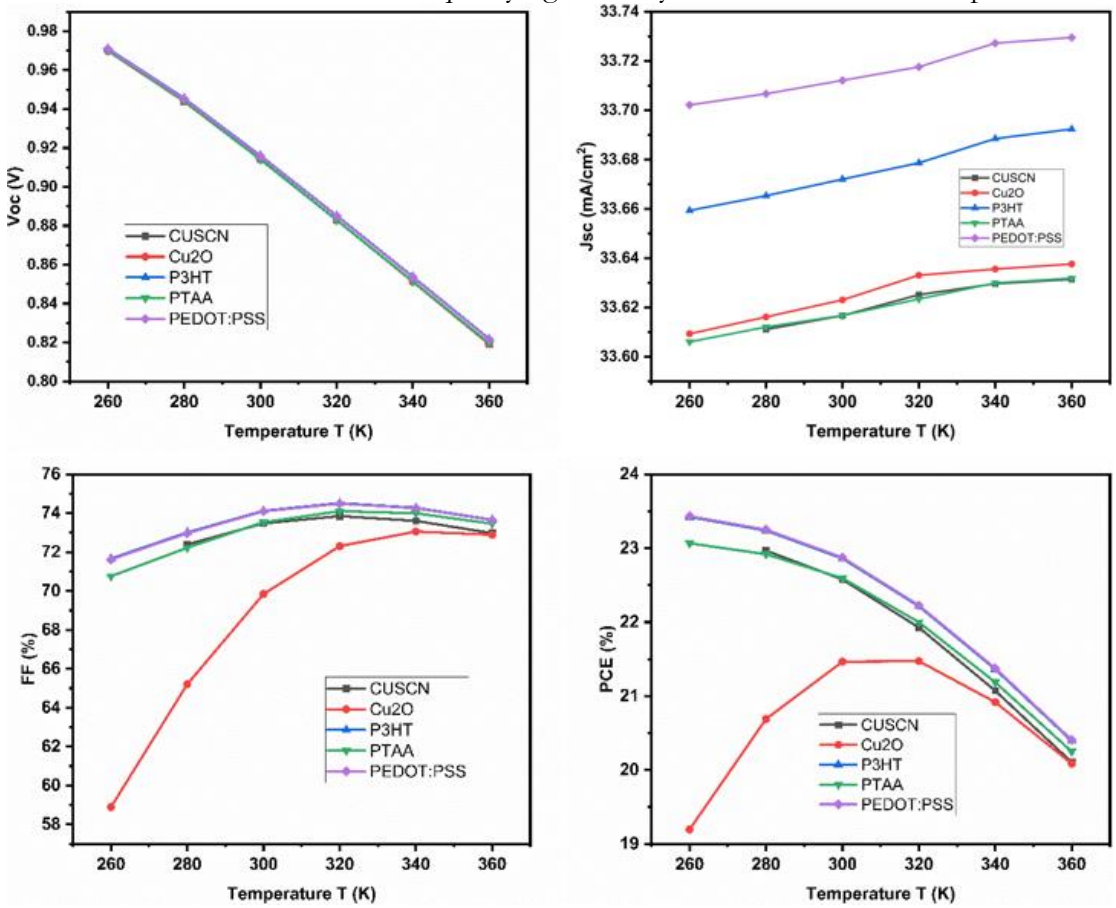


Figure 23. Temperature-Dependent Performance Characteristics of $RbSnBr_3$ Solar Cells

Figure 23 illustrates how temperature variation affects the performance of the devices. As the temperature increases from 260 to 360 K, J_{SC} remains relatively stable across all HTLs, staying around 33.6–33.7 mA/cm², indicating that the simulated photogeneration current is comparatively insensitive to temperature over the investigated range. In contrast, V_{OC} shows a significant and consistent decline for all devices, dropping from 0.97 V to 0.82 V, corresponding to a voltage loss of approximately 0.15 V. While the FF shows some improvement or fluctuation depending on the material, the decrease in V_{OC} leads to an overall reduction in PCE, which falls from a peak range of 23.07–23.43% at lower temperatures to approximately 20.09–20.41% at 360 K, corresponding to a reduction of approximately 2.66–3.34 percentage points or roughly 11–14% relative to the respective low-temperature values. These findings suggest that PEDOT:PSS and P3HT exhibit comparable temperature-dependent behaviour and maintain similar simulated photovoltaic performance throughout the investigated temperature range, which is consistent with previous studies reporting improved thermal characteristics of polymer-based transport layers [41]. The stronger sensitivity of VOC compared with JSC indicates that the simulated temperature response is dominated by thermally induced voltage losses rather than changes in photogeneration. The results indicate that increasing temperature mainly reduces VOC, leading to lower PCE under the simulated conditions; however, experimental investigations are required to validate the long-term operational stability of these devices. Importantly, the temperature-dependent SCAPS results should therefore be regarded as an assessment of the predicted electrical response to temperature variation, rather than direct evidence of long-term material or operational stability. The present simulations do not account for experimental ageing processes such as moisture-assisted degradation, oxygen exposure, ion migration, phase instability, electrode degradation, or encapsulation effects. Consequently, no claim of long-term stability is made on the basis of Figure 23 alone, and experimental ageing and degradation studies will be required to establish the actual operational stability of the proposed $RbSnBr_3$ devices.

Beyond the individual parameter analyses, the present study demonstrates that the performance of $RbSnBr_3$-based perovskite solar cells is governed by the combined influence of interface energetics, defect characteristics, carrier transport, and contact engineering rather than by any single material parameter. The integrated evaluation of band alignment, bulk and interface defect densities, density of states, carrier mobility, contact work functions, resistive losses, capacitance, conductance, and temperature-dependent behaviour establishes a systematic relationship between HTL properties and the resulting electrical response of the device under identical simulation conditions. Although PEDOT:PSS exhibited the highest simulated PCE (22.87%), its difference from P3HT (22.86%) is negligible and both polymer-based HTLs therefore demonstrate comparable photovoltaic performance. Consequently, the principal contribution of this work is not the identification of a universally superior HTL, but the establishment of a comprehensive framework explaining how HTL-dependent interface engineering governs carrier extraction, recombination behaviour, defect tolerance and overall device operation in lead-free $RbSnBr_3$ perovskite solar cells.

Comparison Between This Optimized Work and Earlier Research:

Recent SCAPS-based investigations on $RbSnBr_3$ perovskite solar cells have demonstrated that photovoltaic performance strongly depends on the selected device architecture, transport layers, and optimisation strategy. Previously reported structures, including $FTO/TiO_2/RbSnBr_3/PTAA/Au$, achieved a simulated power conversion efficiency (PCE) of 22.53%, whereas higher efficiencies of 29.79% and 33.25% have been reported for $FTO/SnS_2/RbSnBr_3$ and $ITO/WS_2/RbSnBr_3$ devices, respectively, through optimisation of different transport layers and interface properties [6][7]. Since these studies

employed different device architectures, material parameters, and optimisation approaches, comparison based solely on the reported PCE does not provide a reliable assessment of their scientific contribution.

Under the identical simulation conditions employed in the present work, the PEDOT:PSS- and P3HT-based devices achieved simulated PCEs of 22.87% and 22.86%, respectively. The negligible difference between these efficiencies indicates that both polymeric HTLs provide essentially equivalent photovoltaic performance under the investigated conditions. Therefore, the present results should not be interpreted as demonstrating a significant performance advantage of PEDOT:PSS over P3HT. Instead, the comparative analysis shows that both HTLs provide favourable energy-level alignment, efficient hole extraction, and reduced interfacial recombination, making them equally promising candidates for $RbSnBr_3$-based perovskite solar cells.

Unlike previous studies that primarily focused on efficiency optimisation, the present work provides a controlled comparison of five representative inorganic and polymeric HTLs under identical device architecture and simulation conditions. By varying the HTL material while keeping the absorber, ETL, contacts, and operating conditions unchanged, the study evaluates the combined influence of the different HTL properties on interface energetics, carrier transport, recombination behaviour, defect response, and electrical characteristics. [19][42]

Furthermore, the present study extends beyond conventional J–V analysis by integrating investigations of bulk and interface defect densities, density of states, carrier mobility, contact work function, series and shunt resistance, capacitance–voltage (C–V), conductance–voltage (G–V), quantum efficiency, and temperature-dependent characteristics within a single simulation framework. Rather than evaluating these parameters independently, the work establishes their physical correlation with HTL energy-level alignment and interface-controlled device behaviour. This integrated analysis provides a more comprehensive understanding of the mechanisms governing the performance of lead-free $RbSnBr_3$ perovskite solar cells. [18]

Therefore, the principal contribution of this work is not the identification of the highest simulated power conversion efficiency, but the integrated interpretation of how the different HTL properties influence carrier extraction, recombination behaviour, electrical characteristics, and photovoltaic performance under identical simulation conditions. These findings provide theoretical guidance for the rational design, interface optimisation, and future experimental development of environmentally friendly lead-free $RbSnBr_3$ perovskite solar cells.

Conclusion:

This study evaluated the influence of five representative inorganic and polymeric hole transport layers (CuSCN, Cu_2O, P3HT, PTAA, and PEDOT:PSS) on lead-free $RbSnBr_3$ perovskite solar cells using SCAPS-1D under identical device architecture and simulation conditions. The results demonstrate that HTL selection significantly influences interface energetics, carrier transport, recombination behaviour, sensitivity to the assumed defect conditions, and the resulting photovoltaic performance. PEDOT:PSS and P3HT exhibited nearly identical simulated performances, achieving PCEs of 22.87% and 22.86%, respectively, indicating that both polymer-based HTLs are equally promising for $RbSnBr_3$-based devices, whereas PTAA showed intermediate performance and Cu_2O and CuSCN exhibited comparatively lower efficiencies because of less favourable energy-level alignment and increased recombination losses. Beyond the comparison of photovoltaic parameters, the results were interpreted by considering HTL-dependent interface energetics, bulk and interface defect characteristics, carrier mobility, contact properties, electrical response (J–V,

QE, C–V, and G–V), and temperature-dependent behaviour. These results indicate that the observed photovoltaic differences reflect the combined influence of the different HTL properties rather than the effect of a single independently varied material parameter. These findings provide a controlled numerical basis for understanding how HTL-dependent interface properties influence carrier extraction, recombination behaviour, defect response, and electrical performance in $RbSnBr_3$ perovskite solar cells. The contribution of this study is therefore the integrated physical interpretation of these interrelated effects under identical simulation conditions, rather than the introduction of a new numerical modelling methodology or device architecture. Future work should focus on experimental validation, advanced interface passivation, scalable fabrication, and long-term stability investigations, including ageing, moisture resistance, ion migration, and degradation behaviour.

Declaration of Interest Statement:

The authors affirm that they have no conflicts of interest that would have seemed to affect the research presented in this study.

Author Contribution:

Abdul Mateen Arshad: Writing – original draft, Calculations. A. Ali: Project administration, Investigation, Conceptualization, Validation. Mohsin M. Tarar: Writing – review & editing. Mohsin Ali: Validation, Writing. SU Rahman: Calculations, reviewing editing.

Data availability:

Attached is the Supplementary file.

References:

[1] F. Elmourabit, L. Limouny, and S. Dlimi, "Numerical simulation of a triple-cation halide perovskite solar cell achieving over 34% efficiency," *Results Eng.*, vol. 25, p. 103919, Mar. 2025, doi: 10.1016/J.RINENG.2025.103919.

[2] M. Dada and P. Popoola, "Recent advances in solar photovoltaic materials and systems for energy storage applications: a review," *Beni-Suef Univ. J. Basic Appl. Sci. 2023 121*, vol. 12, no. 1, pp. 66-, Jul. 2023, doi: 10.1186/S43088-023-00405-5.

[3] T. Nakajima and K. Sawada, "Discovery of Pb-Free Perovskite Solar Cells via High-ThroughputSimulation on the K Computer," *J. Phys. Chem. Lett.*, vol. 8, no. 19, pp. 4826–4831, Oct. 2017, doi: 10.1021/ACS.JPCLETT.7B02203.

[4] Z. Chen *et al.*, "Single-Crystal MAPbI3 Perovskite SolarCells Exceeding 21% Power Conversion Efficiency," *ACS Energy Lett.*, vol. 4, no. 6, pp. 1258–1259, Jun. 2019, doi: 10.1021/ACSENERGYLETT.9B00847.

[5] W. Ayaydah, E. Raddad, and Z. Hawash, "Sn-Based Perovskite Solar Cells towards High Stability and Performance," *Micromachines 2023, Vol. 14, Page 806*, vol. 14, no. 4, p. 806, Mar. 2023, doi: 10.3390/MI14040806.

[6] B. K. Ravidas, M. K. Roy, and D. P. Samajdar, "Design Insights and Photovoltaic Performance Analysis of Non-Lead Inorganic RbSnX3 (X = I, Br, Cl) Perovskites through Coupled Density Functional Theory and SCAPS-1D Simulation Frameworks," *ACS Appl. Electron. Mater.*, vol. 6, no. 7, pp. 5126–5150, Jul. 2024, doi: 10.1021/ACSAELM.4C00670.

[7] M. S. Reza *et al.*, "Enhancing RbSnBr3 perovskite solar cells performances: machine learning-driven optimization of active layers and electron transport materials using SCAPS-1D," *Eur. Phys. J. Plus 2025 14010*, vol. 140, no. 10, pp. 990-, Oct. 2025, doi: 10.1140/EPJP/S13360-025-06937-2.

[8] N. L. Dey *et al.*, "Optimization of Sr3NCl3-based perovskite solar cell performance through the comparison of different electron and hole transport layers," *J. Phys. Chem. Solids*, vol. 196, p. 112386, Jan. 2025, doi: 10.1016/J.JPCS.2024.112386.

[9] Y. Gan *et al.*, "Numerical Simulation of High-Performance CsPbI3/FAPbI3 Heterojunction Perovskite Solar Cells," *Energies 2022, Vol. 15, Page 7301*, vol. 15, no.

19, p. 7301, Oct. 2022, doi: 10.3390/EN15197301.

[10] S. A. Dar and B. S. Sengar, "Optimization and Performance Analysis of InorganicLead-Free CsSnBr3 Perovskite Solar Cells Using DiverseElectron Transport Materials," *Energy & Fuels*, vol. 38, no. 9, pp. 8229–8248, May 2024, doi: 10.1021/ACS.ENERGYFUELS.4C00953.

[11] A. Umar *et al.*, "High Power-Conversion Efficiency of Lead-Free Perovskite Solar Cells: A Theoretical Investigation," *Micromachines 2022, Vol. 13, Page 2201*, vol. 13, no. 12, p. 2201, Dec. 2022, doi: 10.3390/MI13122201.

[12] Y. Wang *et al.*, "PTAA as Efficient Hole Transport Materials in Perovskite Solar Cells: A Review," *Sol. RRL*, vol. 6, no. 8, p. 2200234, Aug. 2022, doi: 10.1002/SOLR.202200234;WGROUP:STRING:PUBLICATION.

[13] G. G. Njema, J. K. Kibet, N. Rono, and C. C. Ahia, "Numerical simulation of a novel high performance solid-state dye-sensitised solar cell based on N719 dye," *IET Optoelectron.*, vol. 18, no. 4, pp. 96–120, Aug. 2024, doi: 10.1049/OTE2.12118;JOURNAL:JOURNAL:17518776.

[14] M. S. Reza, A. Ghosh, M. S. Reza, S. Sultana, N. S. Awwad, and H. A. Alturaifi, "Strategic design and evaluation of charge transport layers for high-efficiency lead-free BeSiP2-based perovskite solar cells: A careful examination into electron and hole transport layers," *Sol. Energy*, vol. 287, Feb. 2025, doi: 10.1016/J.SOLENER.2024.113210.

[15] M. Shamim Reza *et al.*, "Boosting the effectiveness of a cutting-edge Ca3NCl3 perovskite solar cell by fine-tuning the hole transport layer," *Mater. Sci. Eng. B*, vol. 309, p. 117656, Nov. 2024, doi: 10.1016/J.MSEB.2024.117656.

[16] T. Feeney *et al.*, "Understanding and exploiting interfacial interactions between phosphonic acid functional groups and co-evaporated perovskites," *Matter*, vol. 7, no. 6, pp. 2066–2090, Jun. 2024, doi: 10.1016/J.MATT.2024.02.004.

[17] A. A. A. Torimtubun, J. G. Sanchez, J. Pallares, and L. F. Marsal, "Photostability Study of Inverted Polymer Solar Cells under AM 1.5G and LED Illumination via Impedance Spectroscopy," *IEEE J. Electron Devices Soc.*, vol. 9, pp. 484–491, 2021, doi: 10.1109/JEDS.2021.3052719.

[18] C. M. Wolff, P. Caprioglio, M. Stolterfoht, and D. Neher, "Nonradiative Recombination in Perovskite Solar Cells: The Role of Interfaces," *Adv. Mater.*, vol. 31, no. 52, p. 1902762, Dec. 2019, doi: 10.1002/ADMA.201902762.

[19] M. Noman, A. H. H. Khan, and S. T. Jan, "Interface engineering and defect passivation for enhanced hole extraction, ion migration, and optimal charge dynamics in both lead-based and lead-free perovskite solar cells," *Sci. Reports 2024 141*, vol. 14, no. 1, pp. 5449-, Mar. 2024, doi: 10.1038/s41598-024-56246-4.

[20] Z. ul Abdin, I. Qasim, O. Ahmad, and M. Rashid, "Numerical modelling analysis of (FA)0.85Cs0.15Pb(I0.85 Br0.15)3: (FAPI)-based perovskite solar cell with different ETMs using solar capacitance simulator," *Sol. Energy*, vol. 228, pp. 100–119, Nov. 2021, doi: 10.1016/J.SOLENER.2021.09.054.

[21] M. O. Reese *et al.*, "Consensus stability testing protocols for organic photovoltaic materials and devices," *Sol. Energy Mater. Sol. Cells*, vol. 95, no. 5, pp. 1253–1267, May 2011, doi: 10.1016/J.SOLMAT.2011.01.036.

[22] M. S. Reza *et al.*, "New highly efficient perovskite solar cell with power conversion efficiency of 31% based on Ca3NI3 and an effective charge transport layer," *Opt. Commun.*, vol. 561, p. 130511, Jun. 2024, doi: 10.1016/J.OPTCOM.2024.130511.

[23] S. M. Seyed-Talebi, M. Mahmoudi, and C. H. Lee, "A Comprehensive Study of CsSnI3-Based Perovskite Solar Cells with Different Hole Transporting Layers and Back Contacts," *Micromachines*, vol. 14, no. 8, p. 1562, Aug. 2023, doi:

10.3390/MI14081562.

[24] M. S. S. Basyoni *et al.*, "On the Investigation of Interface Defects of Solar Cells: Lead-Based vs Lead-Free Perovskite," *IEEE Access*, vol. 9, pp. 130221–130232, 2021, doi: 10.1109/ACCESS.2021.3114383.

[25] Á. Morales-García, R. Valero, and F. Illas, "An Empirical, yet Practical Way To Predict the BandGap in Solids by Using Density Functional Band Structure Calculations," *J. Phys. Chem. C*, vol. 121, no. 34, pp. 18862–18866, Aug. 2017, doi: 10.1021/ACS.JPCC.7B07421.

[26] "Current Density Mismatch in Perovskite Solar Cells," 2020, doi: 10.1021/acsenergylett.0c01642.

[27] L. V. Mercaldo *et al.*, "Procedure Based on External Quantum Efficiency for Reliable Characterization of Perovskite Solar Cells," *Energy Technol.*, vol. 10, no. 10, p. 2200748, Oct. 2022, doi: 10.1002/ENTE.202200748.

[28] I. M. Dharmadasa, Y. Rahaq, A. A. Ojo, and T. I. Alanazi, "Perovskite solar cells: a deep analysis using current–voltage and capacitance–voltage techniques," *J. Mater. Sci. Mater. Electron. 2018 302*, vol. 30, no. 2, pp. 1227–1235, Nov. 2018, doi: 10.1007/S10854-018-0390-5.

[29] S. Zhou *et al.*, "Insight into theStructural, Optical and MechanicalProperties of RbSnX3 (X = Cl, Br, I) under High Pressure," *J. Phys. Chem. C*, vol. 127, no. 27, pp. 13346–13355, Jul. 2023, doi: 10.1021/ACS.JPCC.3C02729.

[30] C. N. M Ouma, K. O. Obodo, M. Braun, M. O. Onani, and F. B. Dejene, "In Silico Insights into the Tunable Magnetic Properties of Transition Metal Doped Monolayer SnS2," *2018 Open Innov. Conf. OI 2018*, pp. 120–123, Nov. 2018, doi: 10.1109/OI.2018.8535869.

[31] M. S. Chowdhury *et al.*, "Effect of deep-level defect density of the absorber layer and n/i interface in perovskite solar cells by SCAPS-1D," *Results Phys.*, vol. 16, p. 102839, Mar. 2020, doi: 10.1016/J.RINP.2019.102839.

[32] R. Chen and C. Persson, "Band-edge density-of-states and carrier concentrations in intrinsic and p-type CuIn1-xGaxSe2," *J. Appl. Phys.*, vol. 112, no. 10, Nov. 2012, doi: 10.1063/1.4767120/368985.

[33] S. K. Vasheghani Farahani *et al.*, "Valence-band density of states and surface electron accumulation in epitaxial <math xmlns="http://www.w3.org/1998/Math/MathML"><msub><mi>SnO</mi><mn>2</mn></msub></math> films," *Phys. Rev. B*, vol. 90, no. 15, p. 155413, Oct. 2014, doi: 10.1103/PhysRevB.90.155413.

[34] J. T. Shieh, C. H. Liu, H. F. Meng, S. R. Tseng, Y. C. Chao, and S. F. Horng, "The effect of carrier mobility in organic solar cells," *J. Appl. Phys.*, vol. 107, no. 8, Apr. 2010, doi: 10.1063/1.3327210/389883.

[35] M. Saadat and S. Bameri, "Comprehensive analysis of transport layers and interface defects in MAPbI3 based PSCs for enhanced efficiency," *Discov. Appl. Sci. 2025 75*, vol. 7, no. 5, pp. 440-, May 2025, doi: 10.1007/S42452-025-06948-9.

[36] J. Schuster, R. E. DeWames, E. A. DeCuir, E. Bellotti, and P. S. Wijewarnasuriya, "Junction optimization in HgCdTe: Shockley-Read-Hall generation-recombination suppression," *Appl. Phys. Lett.*, vol. 107, no. 2, p. 23502, Jul. 2015, doi: 10.1063/1.4926603/29628.

[37] M. F. Ali and M. F. Hossain, "Influence of Front and Back Contacts on Photovoltaic Performances of p-n Homojunction Si Solar Cell: Considering an Electron-Blocking Layer," *Int. J. Photoenergy*, vol. 2017, no. 1, p. 7415851, Jan. 2017, doi: 10.1155/2017/7415851.

[38] T. Minemoto and M. Murata, "Impact of work function of back contact of perovskite

solar cells without hole transport material analyzed by device simulation," *Curr. Appl. Phys.*, vol. 14, no. 11, pp. 1428–1433, Nov. 2014, doi: 10.1016/J.CAP.2014.08.002.

[39] N. Mundhaas *et al.*, "Series Resistance Measurements of Perovskite Solar Cells Using Jsc–Voc Measurements," *Sol. RRL*, vol. 3, no. 4, p. 1800378, Apr. 2019, doi: 10.1002/SOLR.201800378

[40] R. H. Sardar, A. Bera, S. Chattopadhyay, S. I. Ali, S. Pramanik, and A. C. Mandal, "The impact of series (Rs) and shunt resistances (Rsh) on solar cell parameters to enhance the photovoltaic performance of f-PSCs," *Opt. Mater. (Amst).*, vol. 155, p. 115818, Sep. 2024, doi: 10.1016/J.OPTMAT.2024.115818.

[41] P. Singh and N. M. Ravindra, "Temperature dependence of solar cell performance—an analysis," *Sol. Energy Mater. Sol. Cells*, vol. 101, pp. 36–45, Jun. 2012, doi: 10.1016/J.SOLMAT.2012.02.019.

[42] F. H. Isikgor, S. Zhumagali, L. V. Luis, M. De Bastiani, I. McCulloch, and S. De Wolf, "Molecular engineering of contact interfaces for high-performance perovskite solar cells," *Nat. Rev. Mater. 2022 82*, vol. 8, no. 2, pp. 89–108, Nov. 2022, doi: 10.1038/s41578-022-00503-3.

Copyright © by authors and 50Sea. This work is licensed under Creative Commons Attribution 4.0 International License.